Chapter 6 Numerical Simulations

6.1 Introduction

Numerical simulations of limestone behavior under drained and undrained boundary conditions are presented in this chapter. The ability of the 14-parameter cap model to simulate the basic drained behavior of limestone is demonstrated by comparing calculated responses of hydrostatic, uniaxial strain, and triaxial compression loadings with measured or recommended limestone responses. In a similar manner, the ability of the finite element code to calculate the undrained behavior of limestone is demonstrated by comparing calculated responses of uniaxial strain loadings with recommended limestone responses. Simulation results are also presented to demonstrate the ability of the code to predict partially-saturated undrained material behavior. Finally, some example calculations are documented that demonstrate the utility of the finite element code in analyzing the stress and strain states of laboratory test specimens.

6.2 Salem Limestone

The limestone simulated in this chapter is commonly referred to as Salem, Bedford, or Indiana limestone. It was extracted from the Salem formation near the community of Bedford, Indiana. Mechanical property tests were conducted on intact specimens of 13.5-percent porosity Salem limestone by the Vermont office of Applied Research Associates. These mechanical property tests included drained and undrained (with pore pressure measurements) hydrostatic loading tests, K_o or uniaxial strain tests, triaxial compression tests, and strain path tests. Laboratory test

data and recommended material properties were obtained from Blouin and Chitty (1988a, 1988b) and Zelasko (1991).

Table 6.1.
Limestone Cap Model Constants

Cap model parameters		
Parameter	**Value**	**Units**
A	750.6	MPa
C	731.5	MPa
B	3.027E-4	1/MPa
K_1	26250	MPa
K_1	0.360	--
K_2	90.0	--
G_i	15750	MPa
G_1	0.12	--
G_2	90.0	--
R_i	1.50	--
R_1	4.0	--
R_2	0.0028	--
W	0.093	--
D	6.95E-4	1/MPa
X_0	-200.	MPa

6.3 Simulations

6.3.1 Process

Prior to numerically simulating limestone behavior under drained or undrained boundary conditions, it was necessary to determine the skeletal or drained behavior of Salem limestone. The 14-parameter cap model, documented in Chapter 4, was fit to recommended drained Salem limestone mechanical properties (Table 6.1). With this model and fit implemented into JAM, drained single-element boundary value problems were conducted to insure the FE code would reproduce the cap model calculations. Once completed, undrained single-element boundary value problems were conducted.

6.3.2 Drained limestone simulations

The following recommended drained Salem limestone mechanical properties were available for fitting: a failure envelope, hydrostatic load and unload behavior, K_o stress-strain behavior, K_o pressure-volume behavior and K_o stress paths, stress-strain curves from triaxial compression tests conducted at several confining stress levels, and strain path data along three different paths.

Typically, a high fidelity fit of both the hydrostatic loading and K_o, or uniaxial strain, responses is impossible to capture with a relatively simple cap model. For this reason, greater emphasis was placed on fitting the uniaxial-strain stress path and stress-strain responses and less

on the hydrostatic loading response. In Figures 6.1-6.3, the calculated drained K_o stress and strain responses from the 14-parameter cap model are compared to the recommended drained K_o behavior. Figure 6.1 compares the drained K_o stress-strain behavior, Figure 6.2 the K_o stress paths, and Figure 6.3 the K_o pressure-volume responses. The quality of the fits are very good. To make these fits, one must compromise between fitting the K_o stress path and the K_o stress-strain behavior. The model K_o stress-strain response breaks over (softens) at a axial stress of approximately 150 MPa. A better match to the stress-strain behavior would require the K_o stress path to break over at a higher value of principal stress difference. Higher fidelity was desired in the K_o stress path.

In Figure 6.4, the calculated drained hydrostatic pressure-volume response of Salem limestone is compared to the recommended behavior. The quality of the fit is not very good since greater emphasis was placed on fitting the K_o behavior. Only a very complicated cap model, with several tens of fitting parameters, would fit both the hydrostatic and K_o behavior of this material.

Drained triaxial compression (TXC) tests at confining pressures of 100 and 400 MPa were also simulated with the cap model. The calculated responses are plotted as principal stress difference versus axial strain and compared to actual test results in Figures 6.5 and 6.6. The quality of the fits is quite good considering the error introduced into the calculations by the lack of fidelity in the calculated hydrostatic pressure-volume response.

6.3.3 Undrained limestone simulations

The following single-element undrained simulations were performed using the Walker-Sternberg EOS for water and a carbonate EOS for the grain solids. The cap model fit to the recommended drained limestone properties modeled the skeletal behavior of the limestone.

An undrained K_o test conducted on a fully-saturated specimen of Salem limestone was simulated with the FE code. The output is compared to the available recommended properties as another method of verifying the FE code. The calculated and recommended stress-strain

responses are compared in a plot of total axial stress versus total axial strain (Figure 6.7). The calculated undrained K_o stress-strain response is softer than the recommended stress-strain response during the loading phase, while during the unloading it is slightly stiffer. The calculated and recommended stress paths are compared in a plot of principal stress difference versus total mean normal stress (Figure 6.8). The correlation between these two is excellent.

The total (solid), effective (short dash) and pore fluid stresses (long dash) for the simulated undrained K_o test are presented in Figure 6.9 in the format of stress versus total volume strain. This figure illustrates that, even in a competent rock such as limestone, a significant portion of the total applied stress is carried by the pore fluid and the peak effective stress is only 20% of the peak total applied stress.

In "conventional" soil mechanics, water and grain solids are often assumed to be incompressible. These assumptions have significant implications with regard to the response of materials during undrained loading. Under undrained or zero volume change boundary conditions, the strength at failure and the effective stress path are unique for a given material with prescribed initial conditions (Lambe and Whitman 1969). This means that the effective stress path is independent of the applied total stress path. A path of zero volume change in an elastic-plastic material implies that the elastic and plastic volume strains are of equal magnitude and opposite sign. To demonstrate that a unique effective stress path is developed, an undrained triaxial compression (TXC) test, i.e., constant radial stress during shear, and an undrained constant mean normal stress (CP) test, i.e., constant mean normal stress during shear, were numerically simulated. The following conditions existed prior to the undrained loading in both simulations: (1) the compressibilities of the water and the grain solids were zero; (2) the nominal effective confining stress in the specimens was 200 MPa, which was generated by a drained hydrostatic loading; and (3) the initial pore fluid pressure was zero. The stresses during the shear loading were applied incrementally until the calculation would not converge under a convergence tolerance of 0.5 percent. The calculated total and effective stress paths for the TXC test (solid

line) and the CP test (dashed line) are presented in Figure 6.10. The effective stress paths from the TXC and CP tests are identical.

Additional undrained calculations were performed to prove that the undrained effective stress paths are not unique when the water and grain solids are compressible. Three undrained TXC tests were simulated with a nominal effective confining stress of 200 MPa and applied back pressures (initial pore fluid pressures) of 0, 100, and 300 MPa, respectively. The results indicate that as the applied back pressure increased from 0 to 300 MPa, the corresponding effective stress paths moved to lower values of effective mean normal stress (Figure 6.11). This response can be explained with the following logic. As the water becomes stiffer with increasing levels of back pressure, equal strain increments within the specimen generate larger increments of pore fluid pressure. Thus, the effective stress paths move to the left in Figure 6.11.

6.3.4 Partially-saturated undrained limestone simulations

The simulations presented in this section demonstrate the ability of the code to predict partially-saturated undrained material behavior and highlight the types of behavior of interest to an engineer performing a material investigation. They depict material responses at several values of initial air porosity and loaded under several different boundary conditions. Responses from undrained hydrostatic compression (HC), uniaxial strain (K_o), K_o load/constant axial strain unload (K_o/BX), and constant radial-stress triaxial compression (TXC) simulations are presented. Changes in the compressibility and in the shear behavior of Salem limestone as a function of air porosity are made evident. Single-element undrained simulations were performed using the Walker-Sternberg EOS for water, a carbonate EOS for the grain solids, and the algorithms developed in Chapter 3 for partially-saturated materials. The cap model, fit to the recommended drained limestone properties, modeled the skeletal behavior of the limestone.

Simulated HC tests were calculated at each of five values of air porosity (0, 1, 2, 3, and 5 percent). The calculated responses are plotted as total mean normal stress versus total volume strain (Figure 6.12), effective mean normal stress versus total volume strain (Figure 6.13), and

pressure versus total volume strain (Figure 6.14). Pressure-volume responses of the partially-saturated limestone load along the drained HC response curve until the point of "lockup" or "void closure" is reached ("X" in Figure 6.14). Prior to void closure, no appreciable pore fluid pressures have developed and consequently the undrained and drained material responses are nominally the same. At void closure, all of the air porosity has been crushed out of the limestone, all of the compressed pore air has diffused into the pore water, and the limestone is in a fully-saturated state. After void closure, the pore fluid pressure and the undrained bulk modulus increase significantly because the now fully-saturated material is less compressible. This means that for a given increment of volume strain, greater pressure is required to deform a fully-saturated limestone composed of solids and water than a partially-saturated limestone composed of solids, water, and air. The pressure-volume response of the zero-percent air-porosity limestone exhibits an initial loading that is stiffer than the response of the partially-saturated materials due to its higher undrained bulk modulus.

In Figure 6.13, the zero-percent air-porosity limestone does not load along the effective stress pressure-volume curve and the curves of the partially-saturated limestone diverge from the drained response curve at void closure. In both cases, the divergence from the drained response curve is due to both the compression of the grains by the pore fluid and the compression of the pore fluid itself. After loading to peak values of mean normal stress, the limestone unloads elastically until the effective mean normal stress state reaches the tension cutoff, i.e., the points labeled A′ through E′ on Figure 6.13. These same points are labeled A through E on the plot of total mean normal stress versus total volume strain (Figure 6.12). When the unloading stresses reach points A′ through C′, there are still significant pore fluid pressures remaining in the limestone. This is illustrated with greater detail in Figure 6.14 for the 1-percent air-porosity simulation. The effective mean normal stress reaches the tension cutoff at B′ when the total mean normal stress reaches the point B. The difference in pressure between points B′ and B is the magnitude of the pore fluid pressure, which for this example is 70 MPa.

Results from five simulated K_o tests are plotted in Figures 6.15-6.20. These simulations were conducted at the same five values of air porosity (0, 1, 2, 3, and 5 percent) as the HC simulations. Figures 6.15 and 6.16 are presented to aid the reader in understanding the partially-saturated response of limestone under K_o boundary conditions. These figures present the total- and effective-axial stress-strain responses and the total and effective stress paths for limestone with an initial air porosity of 2 percent. The results for all of the simulated air porosities are presented as total axial stress versus total axial strain in Figure 6.17, effective axial stress versus total axial strain in Figure 6.18, and as total and effective stress paths in Figures 6.19 and 6.20.

Under uniaxial-strain boundary conditions, partially-saturated limestone loads elastically until the effective stress path contacts the cap (points labeled "Y" on Figures 6.15 and 6.16). While following the drained K_o stress-strain response curve and the drained stress path, the limestone continues to load and accumulates both elastic and plastic strains until void closure is reached (points labeled X). At void closure, all of the air porosity in the limestone has been crushed out and the material is in a fully-saturated state. At axial strains above void closure, the undrained constrained modulus is significantly greater than the drained or skeletal constrained modulus. For a given increment of axial strain, the total axial stresses and the total mean normal stresses increase faster than the effective axial and mean normal stresses. After reaching peak values of axial stress and mean normal stress, the limestone unloads elastically until the effective stress path contacts the extension failure surface at point C′ (Figure 6.16). The coinciding point on the total stress path is labeled point C. After contacting the extension failure surface at C′, the effective stress path moves along the extension failure surface to lower levels of effective mean normal stress. The total stress path moves along an undrained extension failure surface. When the effective axial stress reaches point C′ during unloading (Figure 6.15), there is still pore fluid pressure remaining in the material. The difference in pressure between points C′ and C is the magnitude of the pore fluid pressure, which is 125 MPa in this example.

Results at the other values of initial air porosity exhibit behavior very similar to that presented for the 2-percent air-porosity limestone in Figures 6.15 and 6.16. The total- and effective-axial

stress-strain curves (Figures 6.17 and 6.18) load along the drained K_o stress-strain response curve until void closure. After void closure, all of the total- and effective-axial stress-strain curves diverge due to the increase in pore fluid pressure. The increase in pore fluid pressure produces both grain and pore-fluid compression, which also causes the effective-axial stress-strain response (Figure 6.18) to diverge from the drained axial stress-strain response.

Each of the total stress paths (Figure 6.19) soften with respect to the drained stress path after reaching void closure. This is due to the greater pressures required to deform the fully-saturated limestone. The points labeled A′ through E′ on Figures 6.18 and 6.20 indicate when the effective K_o stress path reaches the extension failure surface. These same points are labeled A through E on the total stress paths in Figure 6.19 and on the plot of total axial stress versus total axial strain in Figure 6.17. Again, after reaching the extension failure surface, the stress paths move along the failure surface to lower levels of mean normal stress[1]. In total stress space, the stress paths move along separate undrained failure surfaces.

Simulated K_o/BX tests were also calculated at five values of air porosity. The results are plotted in Figures 6.21-6.24 as total axial stress versus total axial strain in Figure 6.21 and as total and effective stress paths in Figures 6.23 and 6.24. Figure 6.22, which is a plot of the total and effective stress paths for a 1-percent air-porosity limestone, is presented to aid the reader in understanding the load and unload stress paths produced during a K_o/BX test.

The initial loadings from the K_o/BX simulations are identical to the loading results from the undrained K_o simulations described above. The constant axial strain unloadings (Figure 6.21) drive the limestone along dilatant paths, i.e., ones of forced volumetric expansion. These dilatant paths give rise to total and effective stress paths (Figure 6.23 and 6.24) that initially exhibit increasing values of principal stress difference. These increases are followed by decreasing values of principal stress difference as the effective stress states contact and subsequently move down the drained failure surface. Common points on a set of total and effective stress paths are

[1] It was not possible to further unload the zero-porosity K_o simulation after contacting the extension failure surface.

identified in Figure 6.22. Void closure occurs at point X and thus identifies where the total and effective stress paths diverge due to increasing pore fluid pressures. The end of the K_o loading is identified by points A and A′, and the points B and B′ identify total and effective stress states where the effective stress path contacts the drained failure surface. After contacting the failure surface, the effective stress path moves down the drained failure surface as pressures are decreased.

Simulated TXC tests were calculated at three values of confining pressure (150, 250 and 350 MPa) at each of five values of air porosity (0, 1, 2, 3, and 5 percent). These simulations were conducted to demonstrate the change in undrained strength as a function of both air porosity and confining pressure. The results are plotted in Figures 6.25 through 6.36 in the form of total and effective stress paths, stress-strain curves, and failure surfaces. Total stress paths generated at each of the three confining pressures are plotted in Figures 6.25-6.27. All of the total stress paths load along a 3:1 slope during shear when plotted as principal stress difference versus total mean normal stress. Effective stress paths generated at each of the three confining pressures are plotted in Figures 6.28-6.30. The drained failure envelope (or surface) from the cap model fit of Salem limestone is also plotted in each of these figures.

The response of partially-saturated limestone under TXC boundary conditions is significantly affected by the stress and strain state at which void closure occurs. At a confining pressure of 350 MPa, void closure occurs during the application of confining pressure and prior to the beginning of the shear loading at each of the five values of air porosity. All of the effective stress paths in Figure 6.30 exhibit increasing values of principal stress difference and decreasing values of effective mean normal stress. In contrast, at the 150-MPa confining pressure, void closure only occurs during the application of confining pressure in the materials with initial air porosities of zero and 1 percent. During the initial shear loading, effective stress paths with initial air porosities of 2, 3, and 5 percent (Figure 6.28) load along the drained stress path and then diverge from that path as void closure occurs (points labeled A, B, and C). At the 250-MPa confining pressure, the 5-percent air-porosity limestone reaches void closure during shear at point A in

Figure 6.29, and void closure occurs during the application of confining pressure at the lower air porosities.

The effective stress paths from the fifteen simulations are plotted together in Figure 6.31. The simulations at each confining pressure can be identified by line type, solid lines for the 150-MPa, long dash-short dash lines for the 250-MPa, and dashed lines for the 350-MPa confining pressures. An effective stress path represents a contour or loading path of nominal constant volume. The term nominal is used because some grain and water compression occurs due to increasing pore fluid pressures. One should recall that the strain hardening cap used in the constitutive model is a contour of constant plastic-volume strain. Assuming elastic strains are small, the effective stress paths in Figure 6.31 provide a good approximation of both the cap shape and the change in shape with increasing mean normal stress.

Stress-strain curves from the simulated TXC tests are plotted in Figures 6.32-6.34 for each of the three levels of confining pressure. Axial strains developed during the application of confining pressure were subtracted from all of the stress-strain curves. The stress-strain curves exhibit softer initial loading moduli for materials that were not fully saturated at the start of shear. They also exhibit a noticeable change in loading modulus when void closure occurred during shear.

For each value of air porosity, a portion of an undrained failure surface was drawn by fitting a first or second order curve through the failure point from each of the three total stress paths. All of the undrained failure surfaces, three total stress paths, and the drained failure envelope from the cap model are plotted in Figure 6.35. As expected, each section of undrained failure surface increases in magnitude as the initial air porosity increases. Undrained strength increased by approximately a factor of two as air porosity increased from zero to 5percent.

Pressure-volume responses under HC and TXC boundary conditions are plotted in Figure 6.36 for a 5-percent air-porosity limestone. The TXC simulation was loaded to a confining pressure

of 150 MPa (point X in Figure 6.36) and subsequently loaded in shear (from point X to B) until it would not converge. Under hydrostatic loading boundary conditions, a mean normal stress of approximately 400 MPa is required to reach a volume strain of 5 percent, and a mean normal stress of 230 MPa produces a volume strain of approximately 3 percent (point A in Figure 6.36). However, under TXC boundary conditions, a 5-percent volume strain was produced with only a maximum mean normal stress of 230 MPa (point B in Figure 6.36). The additional volume strain is primarily due to shear induced compaction with a small component due to changing mean normal stress. As the limestone is loaded in shear, the strain hardening cap is pushed out producing additional plastic volume change in the material.

The previous sections show that the FE code can accurately simulate both drained and undrained responses of Salem limestone under ideal laboratory test boundary condition. In the following sections, non-ideal boundary conditions that actually exist in the laboratory tests will be simulated.

6.4 Test Specimen Simulations

6.4.1 FE grid

Cylindrical test specimens were simulated with the axisymmetric FE grid depicted in Figure 6.37. A quarter grid, consisting of 144 elements and 483 nodes, was used in the simulation due to the symmetric nature of the problem. The specimen end caps were included in the simulation to investigate the effects of end cap restraint upon both the stress and strain conditions within the test specimen. A worst case situation was simulated, i.e., one in which no sliding was permitted between the specimen and the steel end caps.

The simulated specimen is 11.43 cm (4.5 in.) in length with a diameter of 5.04 cm (2 in.). The permeability of the limestone was 1.03×10^{-9} m^2, which is a value that insures a uniform pore pressure field throughout the mesh during both the drained and undrained simulations.

6.4.2 Simulation of drained triaxial compression test

A drained triaxial compression test at a confining stress of 200 MPa was simulated in the following manner. First, equal increments of vertical and radial normal stresses were applied to the boundaries of the grid until the stresses equaled 200 MPa. Second, increments of vertical stress were applied until the total vertical stress reached 550 MPa. Finally, increments of vertical stress were removed until a hydrostatic state of total stress was obtained.

The output from this calculation is plotted in the form of contour plots of several stress or strain parameters, i.e., $\sqrt{J_{2D}}$, plastic volume strain, axial strain and radial strain (Figures 6.38 and 6.39). The contour plots present the state of stress or strain in the specimen at the time of peak total vertical stress (Note: the end cap is not included in these contour plots). With the exception of the upper 15 to 20 percent of the specimen, i.e., near the interface of the specimen and end cap, the state of stress within the specimen is relatively uniform (Figure 6.38). This is also true of the plastic volume strains within the specimen (Figure 6.38). However, both the axial and radial strains (Figure 6.39) exhibit significant gradients throughout the specimen. The smallest axial strains (0.03 m/m) are at the top of the specimen; the largest (0.20 m/m) develop at the center of the specimen. The radial strains vary from approximately zero at the specimen-end cap interface to as much as -0.065 m/m at the center of the specimen.

Table 6.2.
Laboratory Calculated Stress and Strain Values

Axial Strain	15.8%
Radial Strain	- 6.2%
Principal Stress Difference	310 MPa
$\sqrt{J_{2D}}$	179 MPa

Table 6.2 contains values of stress and strain that would be calculated from laboratory measured load and deformation measurements. Stresses, e.g., principal stress difference, were corrected for the changing cross-sectional area of the test specimen. The stress values underestimate the strength of the test specimen by approximately 5 percent, 179 MPa (from above table) versus 190 MPa (average stress throughout specimen). The axial strain of

15.8 percent represents only a small portion of the calculated axial strain within the test specimen, while the radial strain of -6.2 percent is representative of the radial strains in the central portion of the test specimen.

This calculation implies that the state of stress within the test specimen is not significantly effected by end cap restraints. Uniform stresses occur throughout major portions of the specimen. In contrast, large axial and radial strain gradients were developed in the test specimen. This implies that some type of end-cap lubrication should be used if uniform states of strain are desired.

6.4.3 Simulation of consolidated undrained triaxial compression test

A consolidated undrained triaxial compression test at a confining stress of 200 MPa was simulated with the FE code JAM. To begin the calculation, equal increments of vertical and radial normal stresses were applied to the boundaries of the grid until a hydrostatic stress of 200 MPa was achieved. During this hydrostatic loading, pore fluid was allowed to drain from the specimen. The boundary conditions were then changed so that no pore fluid could drain from the specimen. Finally, increments of vertical stress were applied until the solution would not converge, which implied that the specimen had failed. Failure occurred at a total axial strain of approximately 4.7 percent. A uniform pore fluid pressure existed throughout the specimen.

The output from this calculation is plotted in the form of contour plots of $\sqrt{J_{2D}}$, volume strain, axial strain, and radial strain (Figures 6.40 and 6.41). The contour plots present the state of stress or strain in the specimen at the time of specimen failure (Note: The end cap is again not included in these contour plots). The $\sqrt{J_{2D}}$ contours (Figure 6.40) illustrate that a uniform state of stress exists within a majority of the test specimen;

Table 6.3.
Laboratory Calculated Stress and Strain Values for Undrained TXC Test

Axial Strain	4.7%
Radial Strain	- 0.4%
Volume Strain	3.8%
Principal Stress Difference	216 MPa
$\sqrt{J_{2D}}$	124 MPa

significant gradients only exist near the specimen-end cap interface. The same is true of the volume strain contours. The calculated volume strains indicate that the specimen was compacting. The calculated pore pressures confirm this observation, i.e., they increase continuously until specimen failure occurs. Due to the small axial strain level at which specimen failure occurs, significant gradients of axial and radial strain were not developed in the test specimen (Figure 6.41). Axial strains vary from 0.02 m/m at the top of the specimen to less than 0.055 m/m in the center of the specimen. Radial strains range from approximately zero at the specimen-end cap interface to -0.004 m/m at the center of the specimen.

Table 6.3 contains values of stress and strain that would be calculated from laboratory measured load and deformation measurements. As in the drained simulation, stresses were corrected for the changing cross-sectional area of the test specimen. The laboratory calculated stress values correspond with the values from the test specimen simulation, i.e., 124 MPa (from above table) versus 123 MPa (average stress throughout specimen). The laboratory calculated volume strain of 3.8 percent underestimates the simulated volume strains that vary between 4 and 4.4 percent throughout most of the test specimen. The axial strain of 4.7 percent agrees with the calculated axial strain throughout a major portion of the test specimen. The radial strain of -0.4% is representative of the simulated radial strains in the central portion of the test specimen.

This calculation demonstrates that significant stress and strain gradients are not developed in the limestone when the specimen fails at small axial strains, despite the introduction of end cap restraint. In addition, the stresses and strains calculated from laboratory measurements correlate well with the actual stress and strain states within the test specimen.

6.5 Summary

Numerical simulations of limestone behavior under drained and undrained boundary conditions were presented in this chapter. The ability of the 14-parameter cap model to simulate the drained behavior of the limestone was demonstrated by comparing calculated responses of

hydrostatic, uniaxial strain, and triaxial compression loadings with measured or recommended limestone responses. The ability of the finite element code to calculate the undrained behavior of the limestone was demonstrated by comparing calculated responses of uniaxial strain loadings with recommended limestone responses. Finally, both drained and undrained TXC test simulations were documented which demonstrate the utility of the finite element code in analyzing laboratory test specimen conditions.

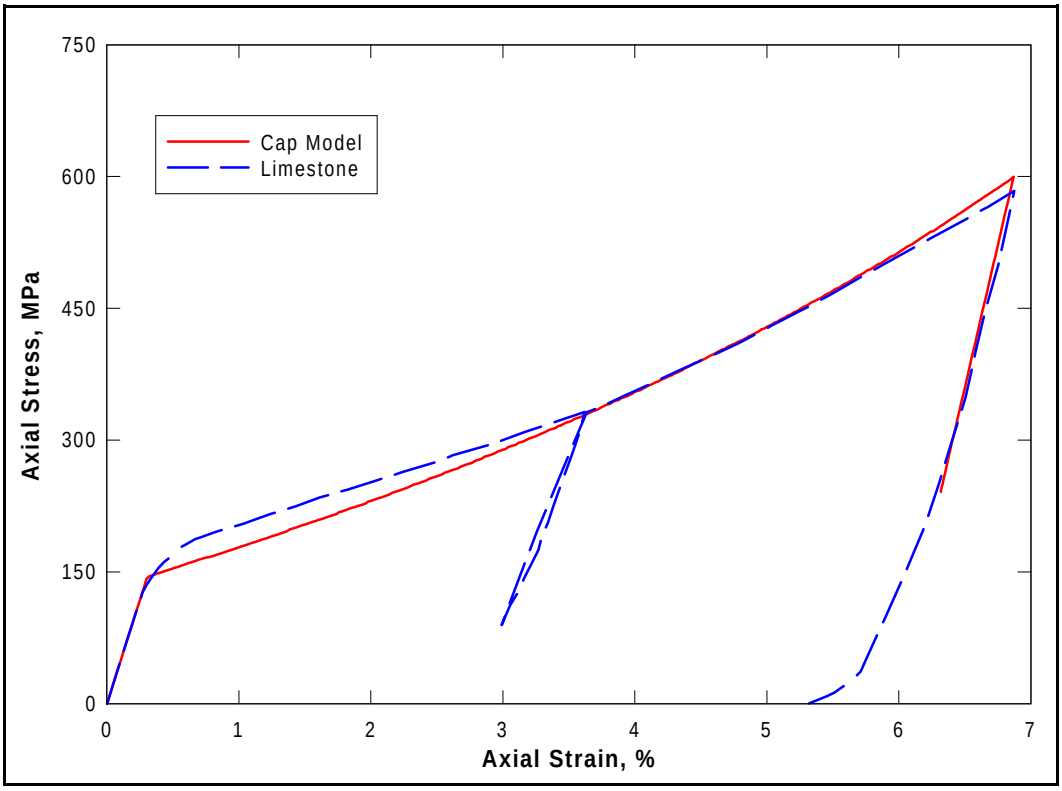

Figure 6.1. Drained K_o stress-strain comparison

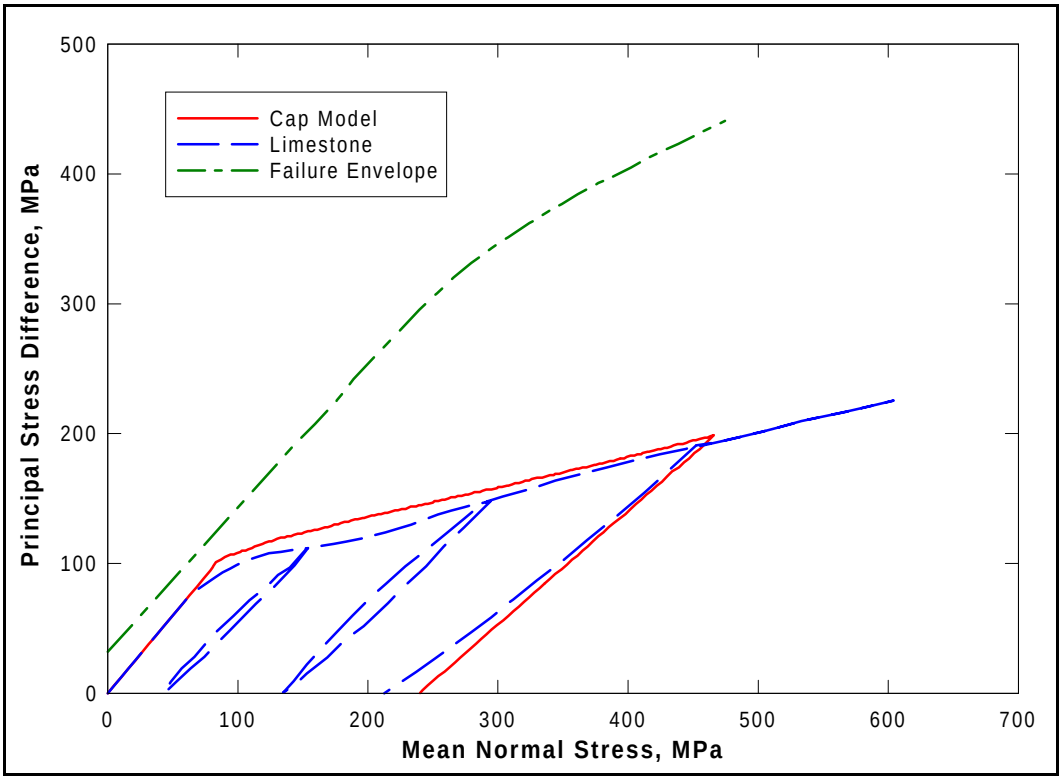

Figure 6.2. Drained K_o stress path comparison

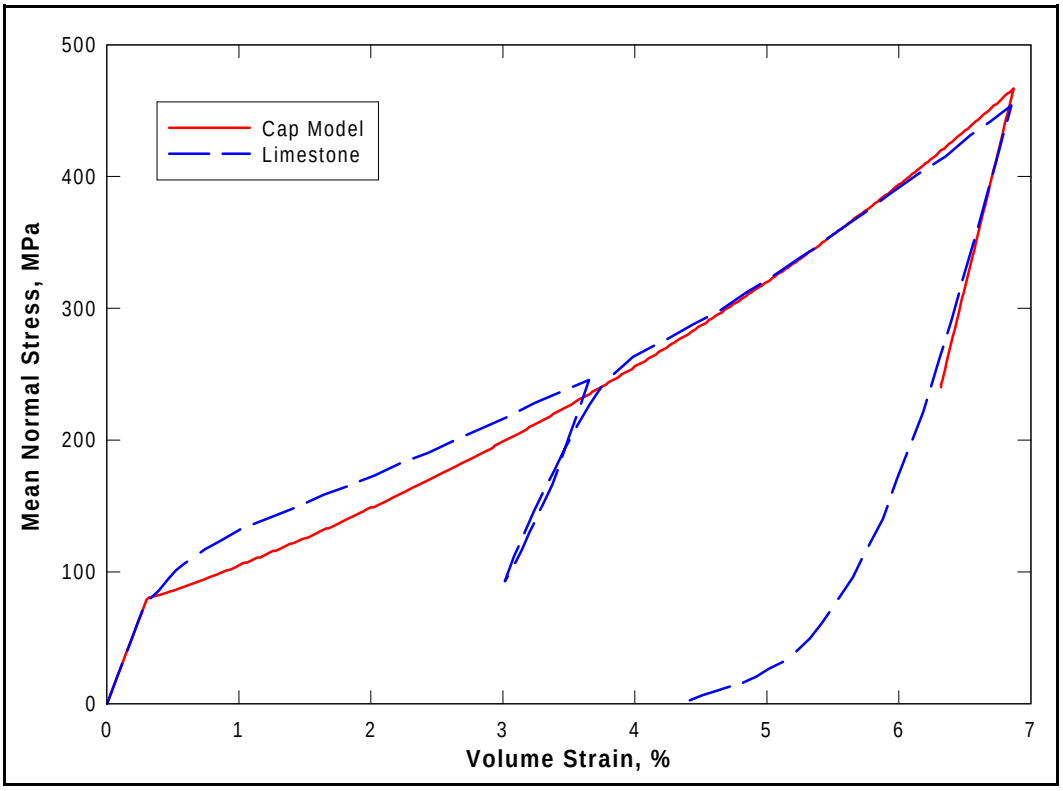

Figure 6.3. Drained K_o pressure-volume comparison

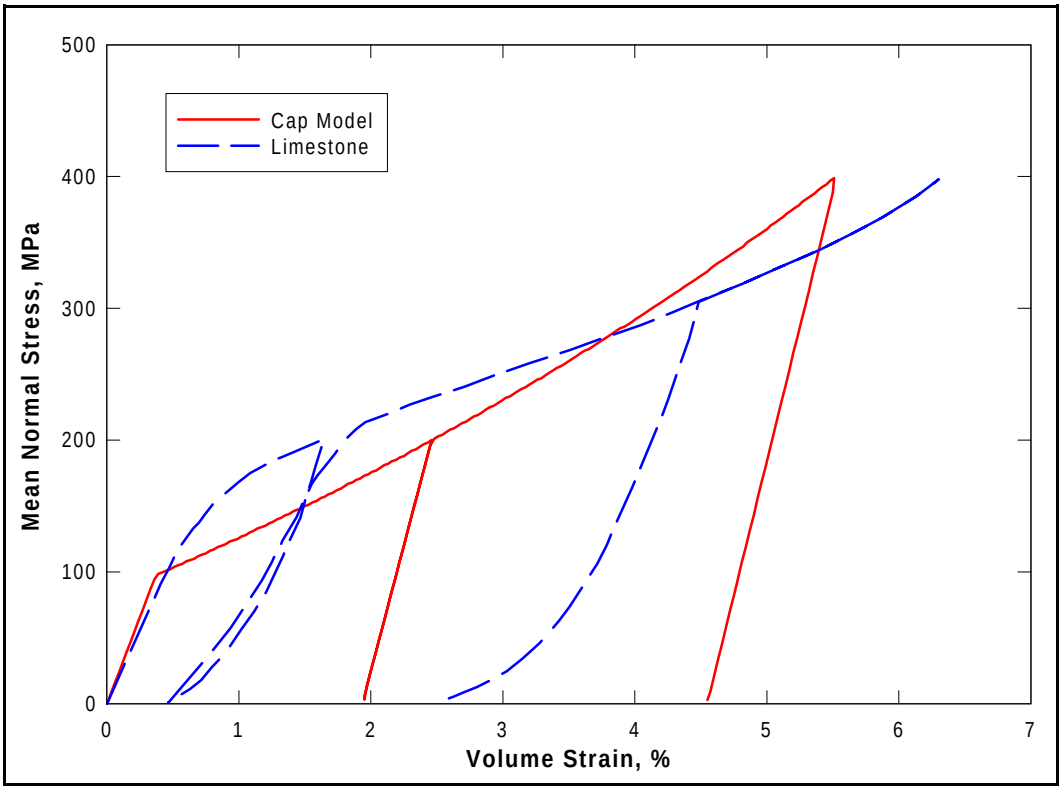

Figure 6.4. Drained hydrostatic load-unload comparison

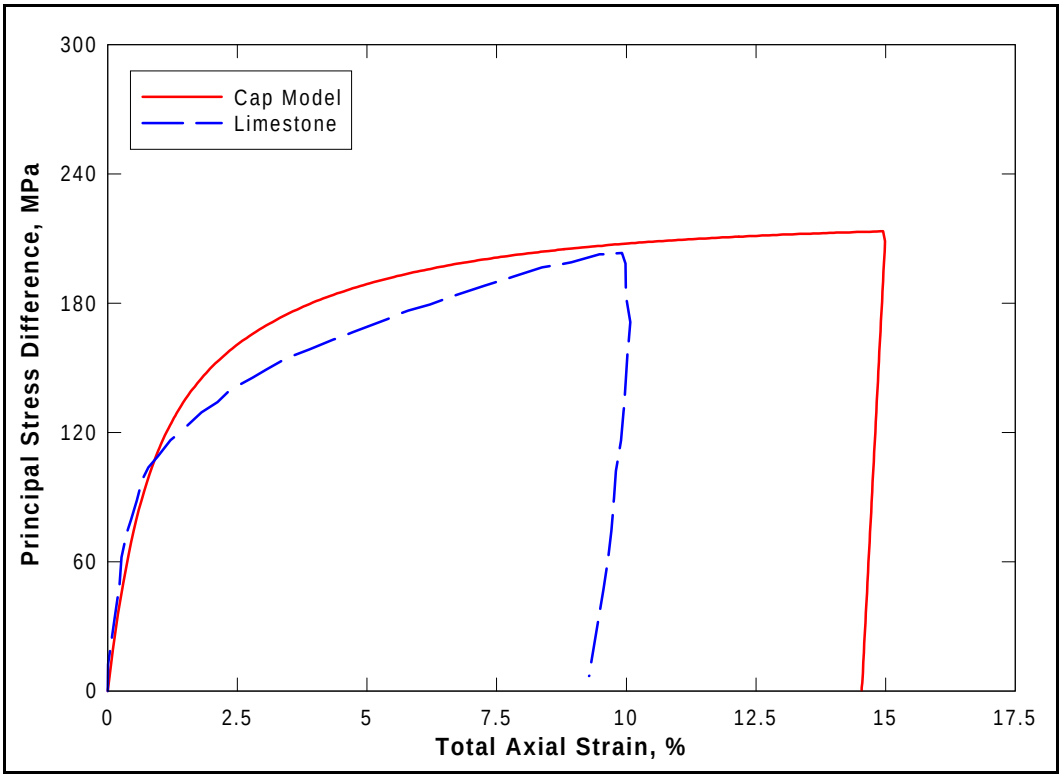

Figure 6.5. Drained TXC stress-strain comparison at 100 MPa confining pressure

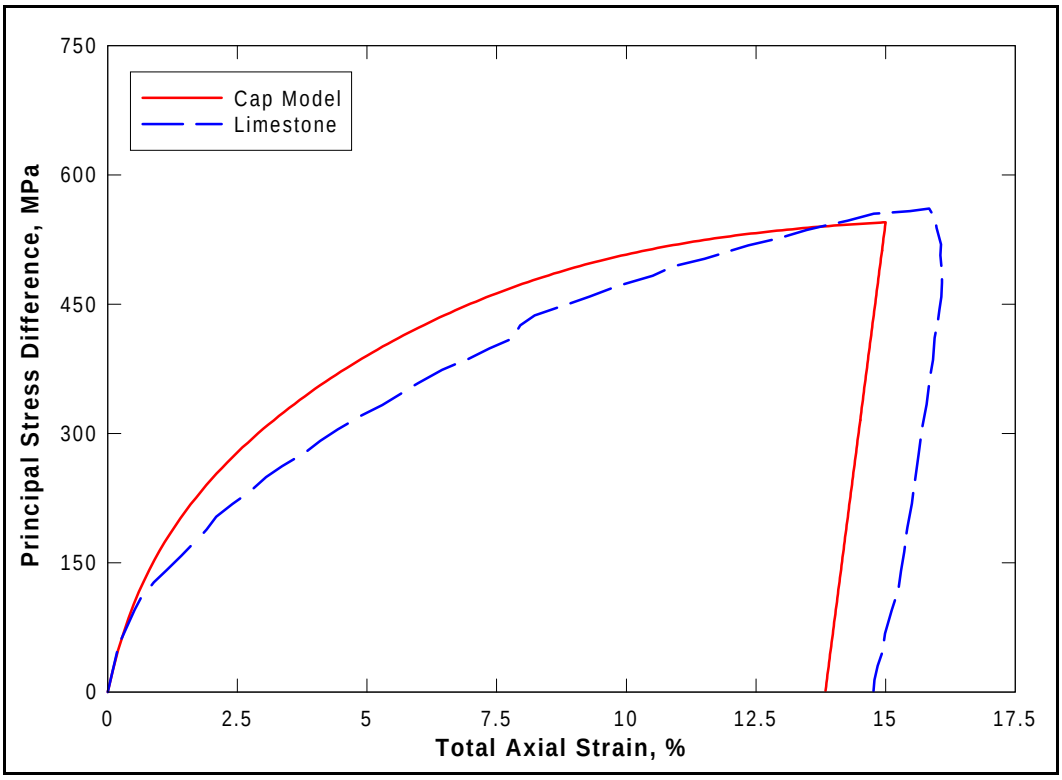

Figure 6.6. Drained TXC stress-strain comparison at 400 MPa confining pressure

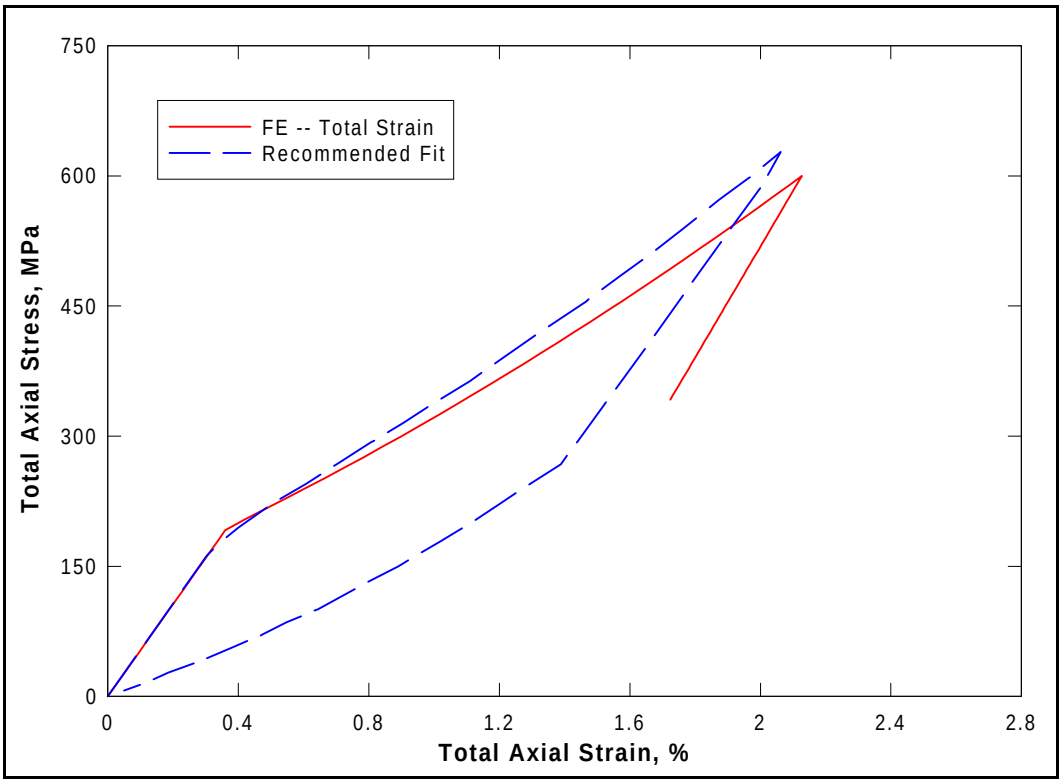

Figure 6.7. Undrained K_o stress-strain comparison

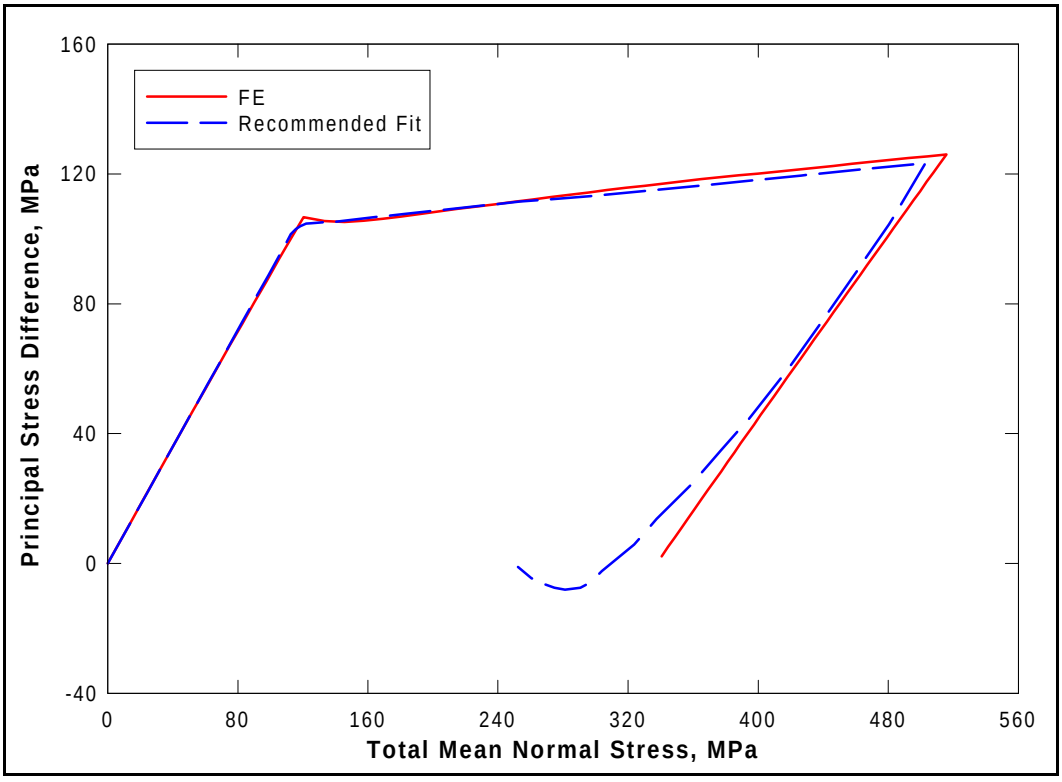

Figure 6.8. Undrained K_o stress path comparison

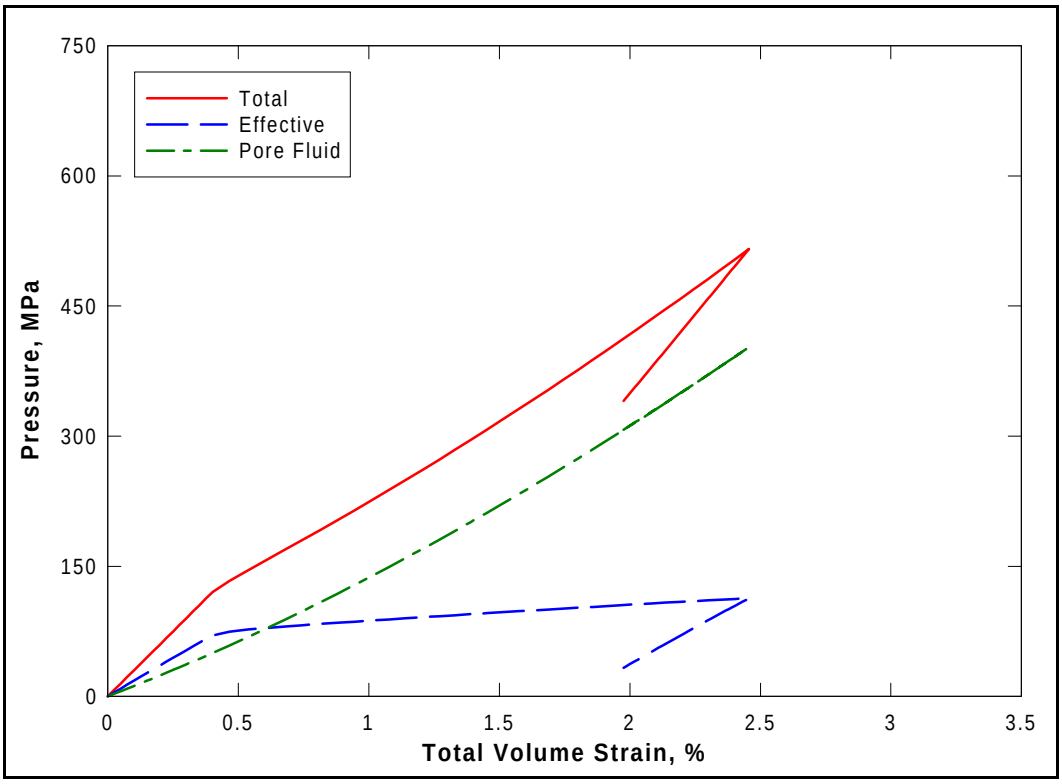

Figure 6.9. Stresses in a simulated undrained K_o test

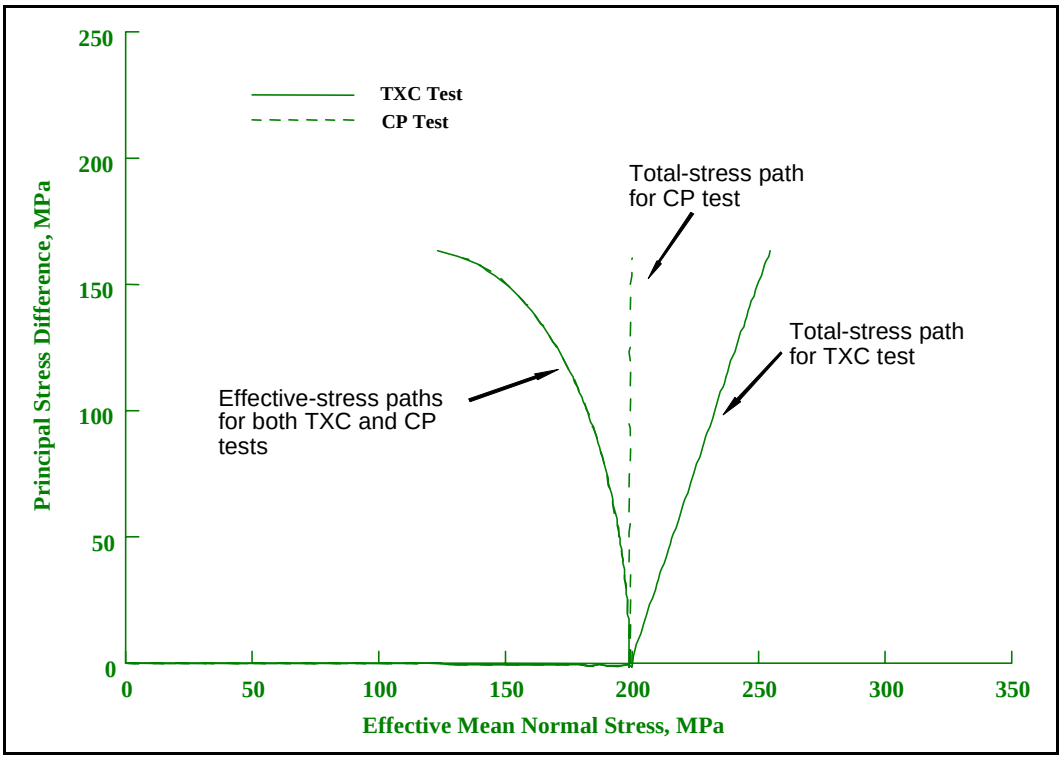

Figure 6.10. Total and effective stress paths from TXC and CP tests

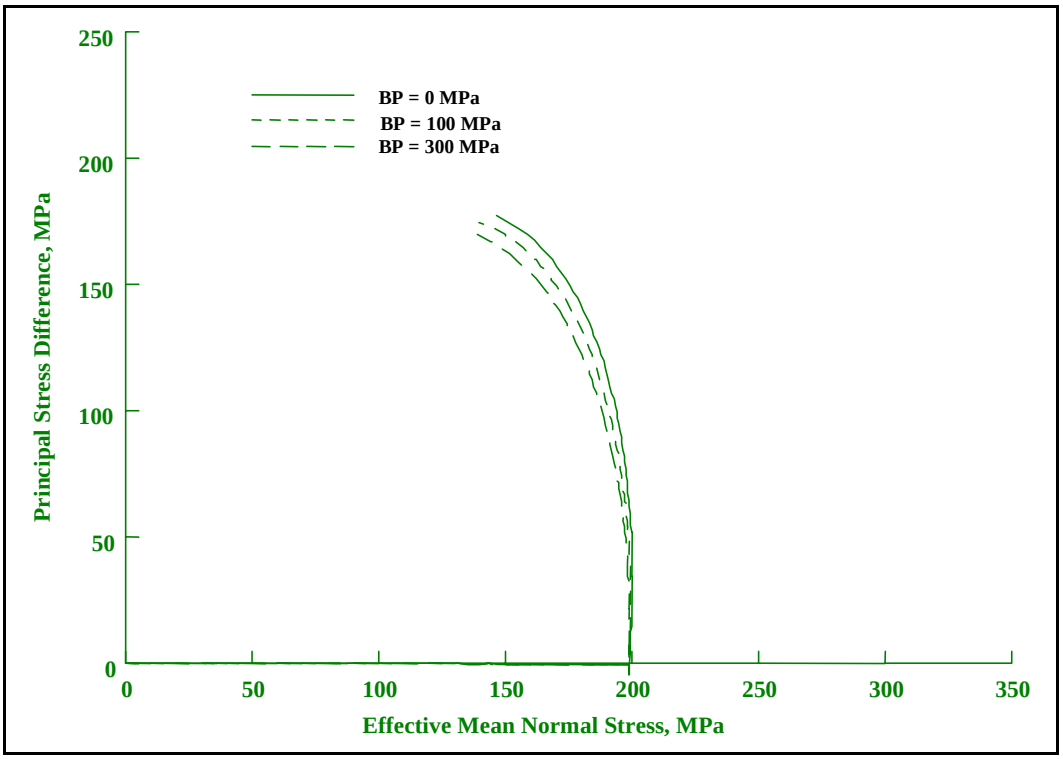

Figure 6.11. Effective stress paths from tests with different back pressures

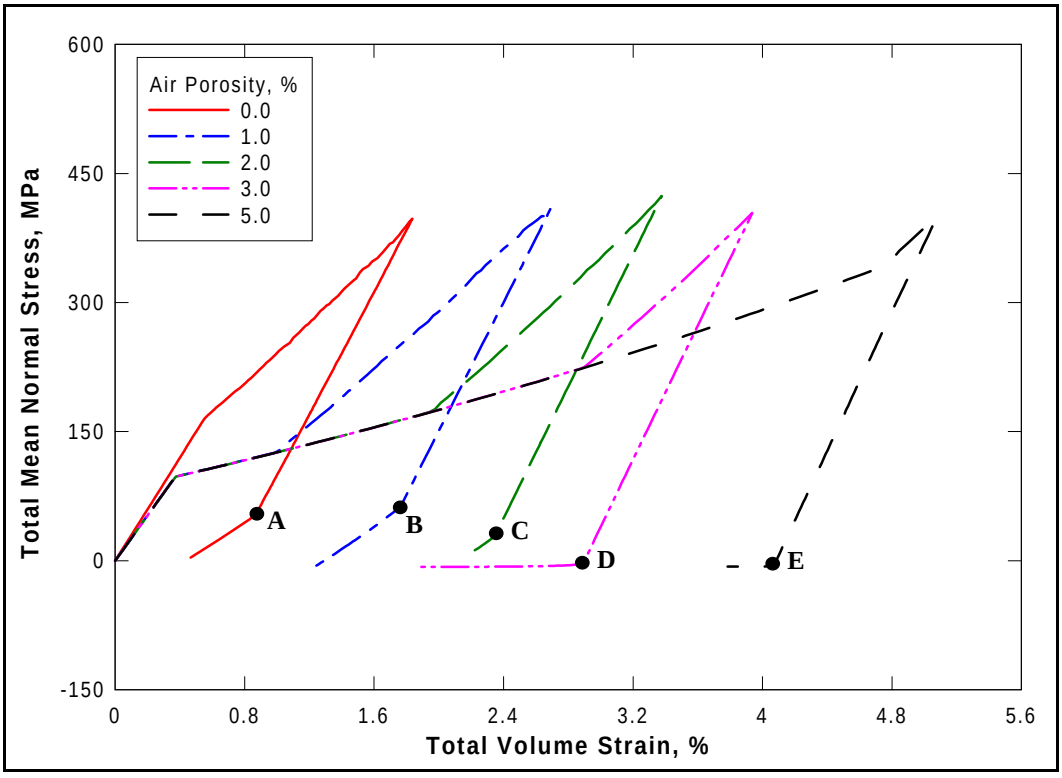

Figure 6.12. Pressure-volume results from five HC simulations

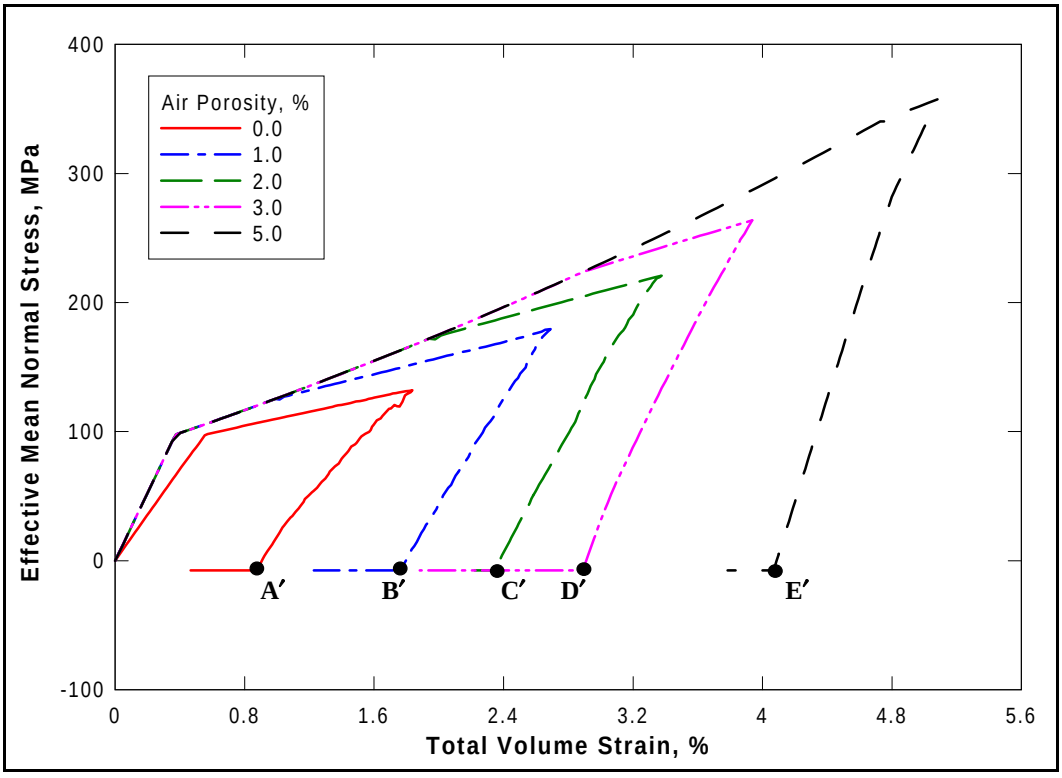

Figure 6.13. Effective pressure-volume results from five HC simulations

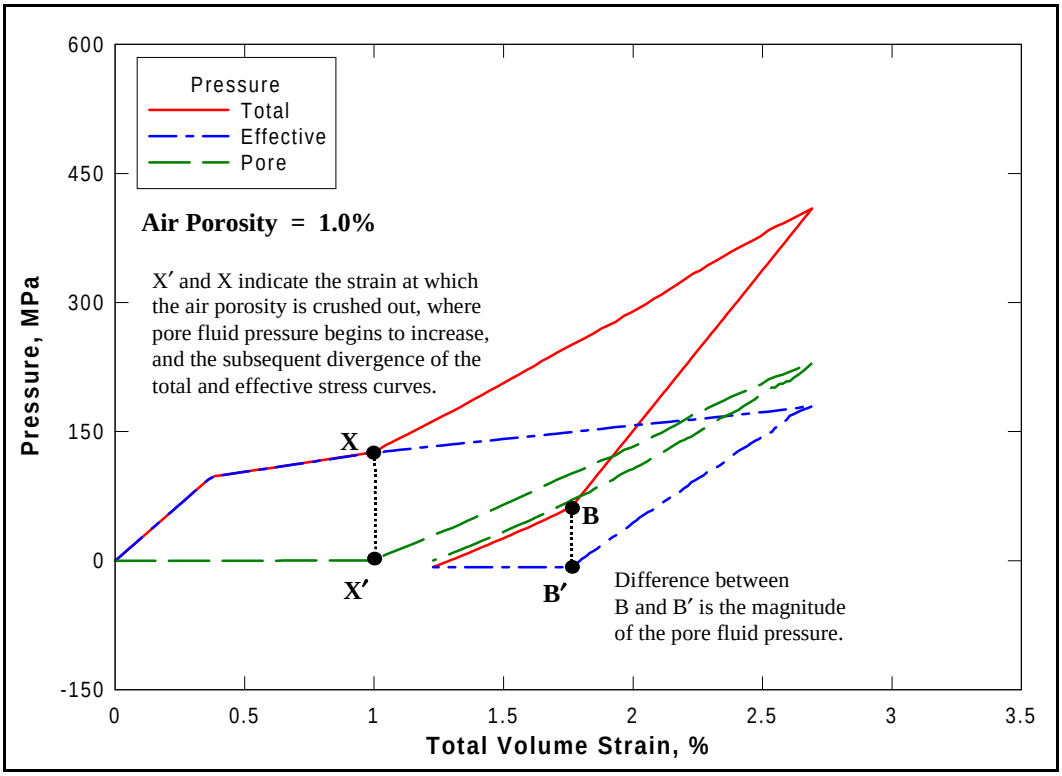

Figure 6.14. Pressure-volume results from HC simulation at 1% air porosity

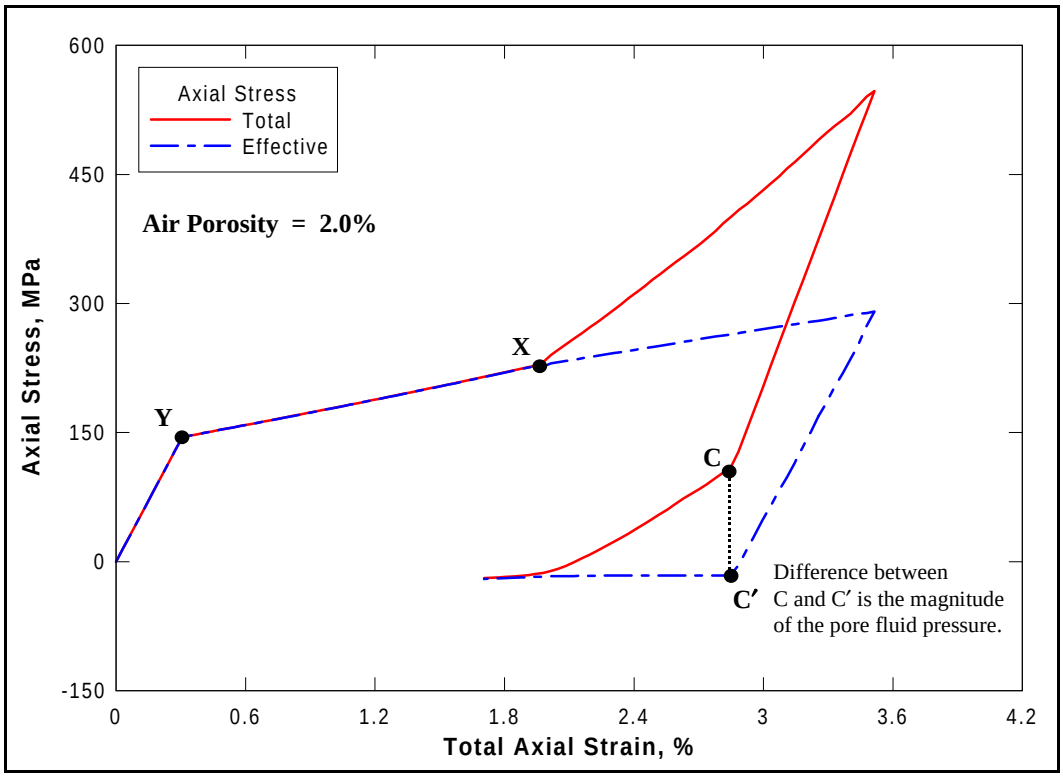

Figure 6.15. Stress-strain results from K_o simulation at 2% air porosity

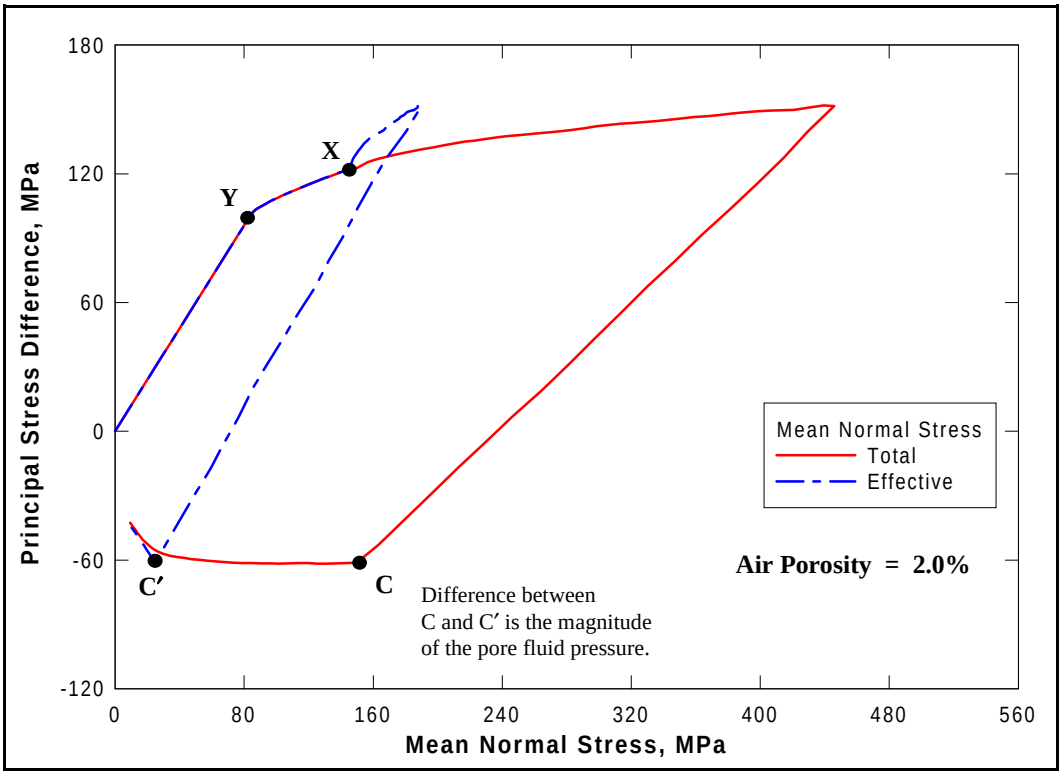

Figure 6.16. Stress paths from K_o simulations at 2% air porosity

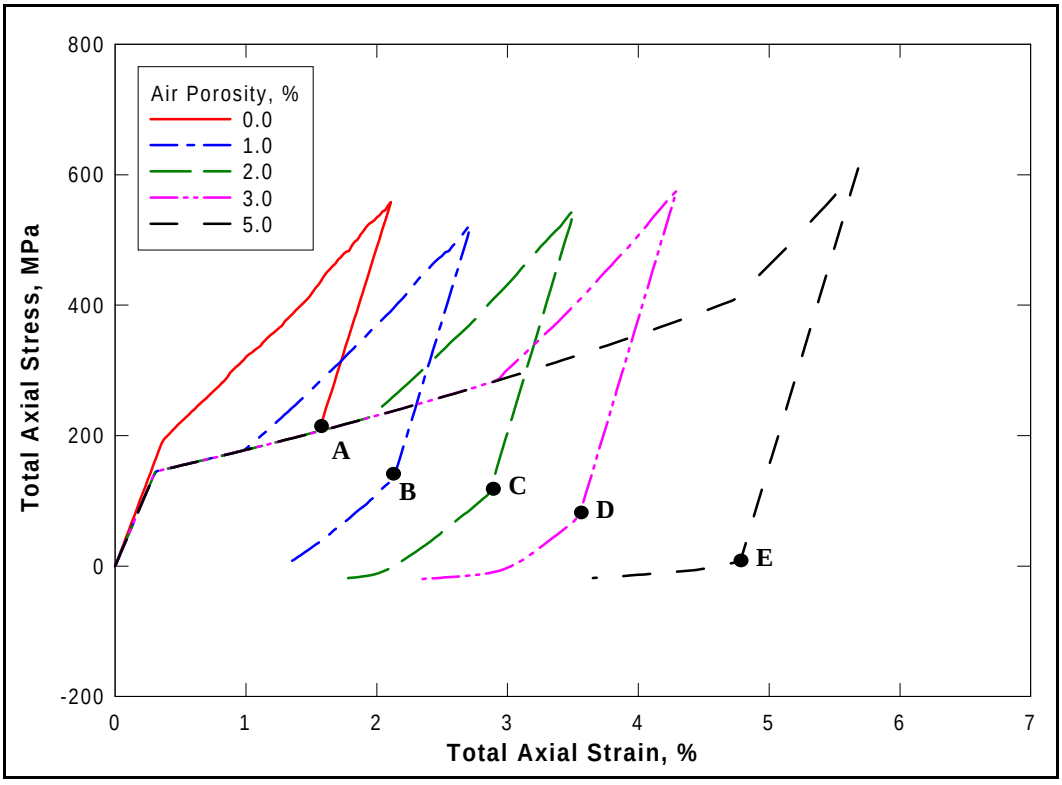

Figure 6.17. Stress-strain results from five K_o simulations

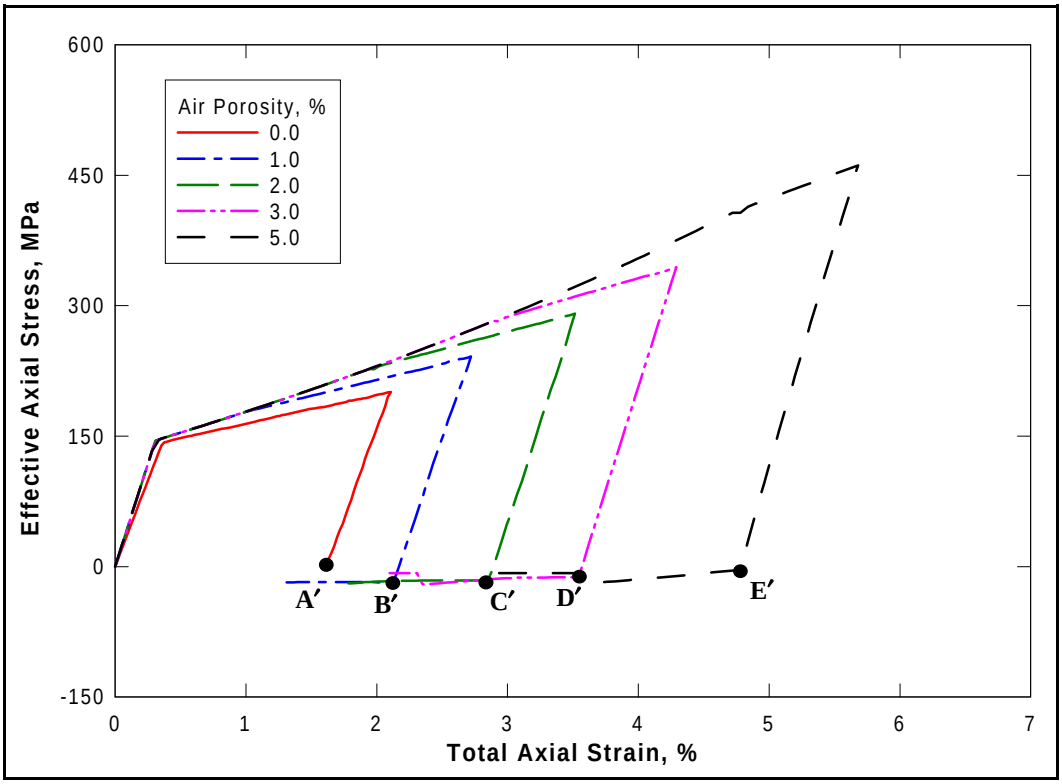

Figure 6.18. Effective stress-strain results from five K_o simulations

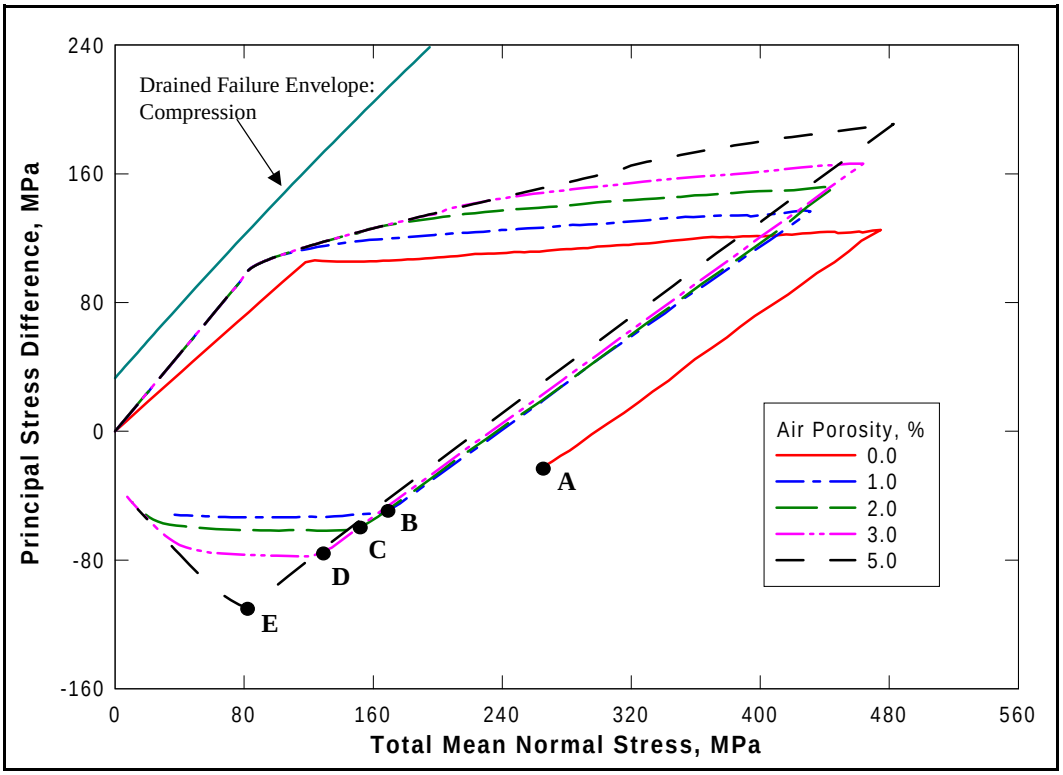

Figure 6.19. Total stress paths from five K_o simulations

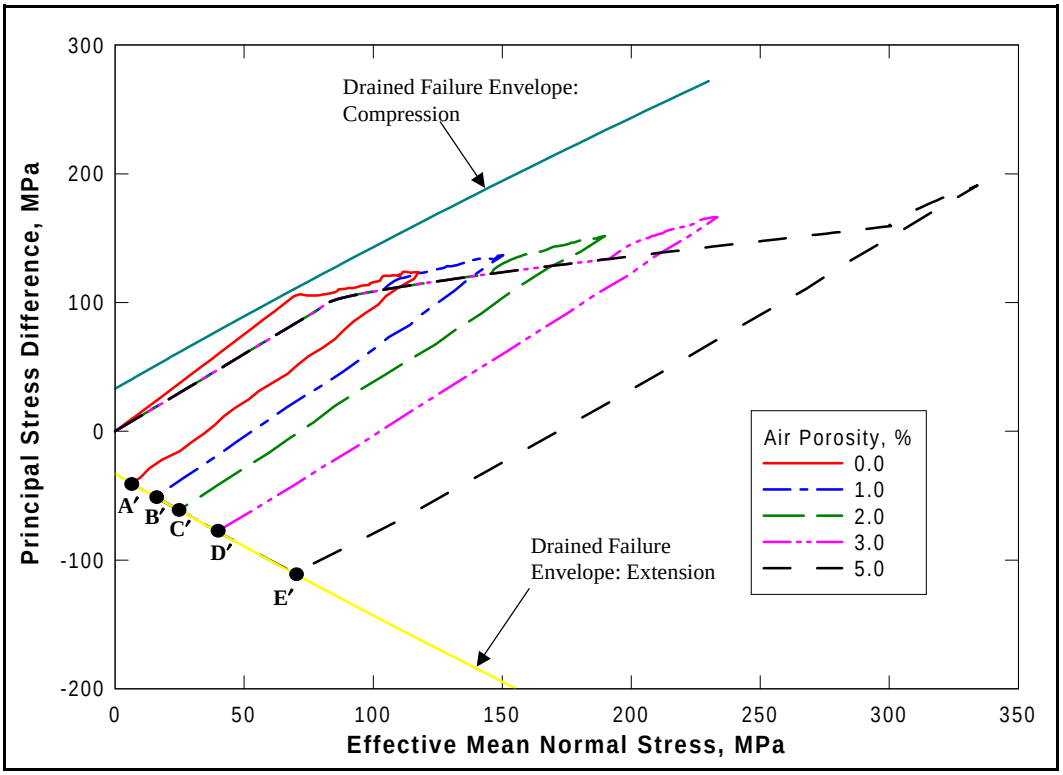

Figure 6.20. Effective stress paths from five K_o simulations

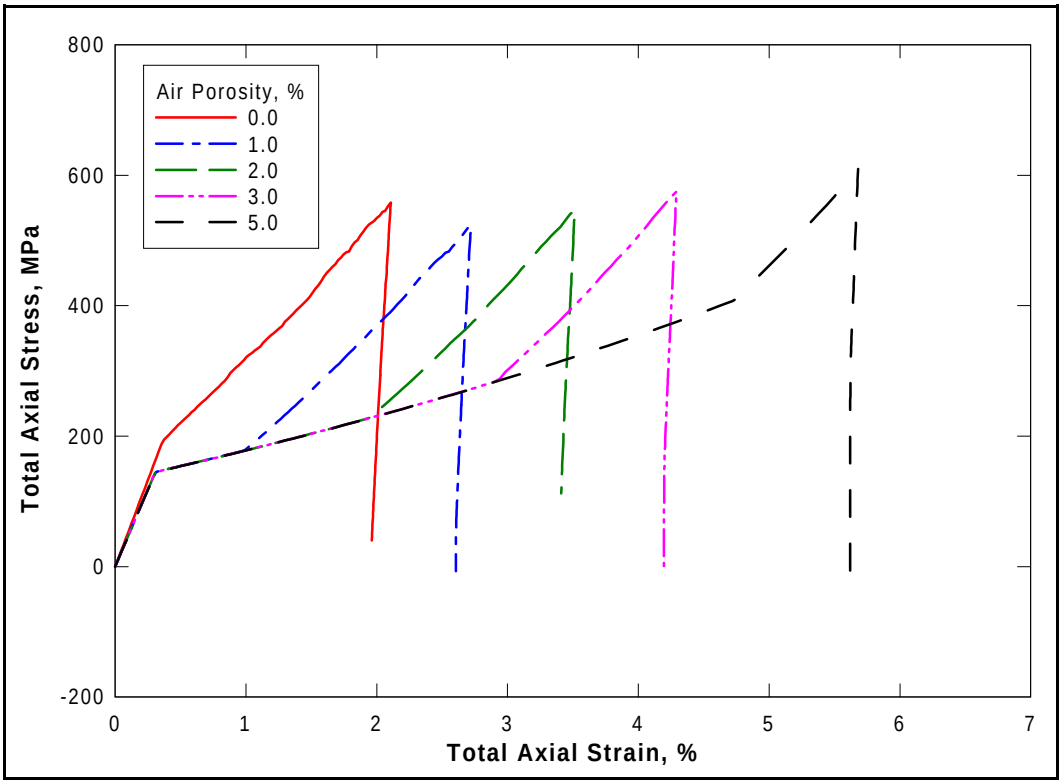

Figure 6.21. Stress-strain results from five K_o/BX simulations

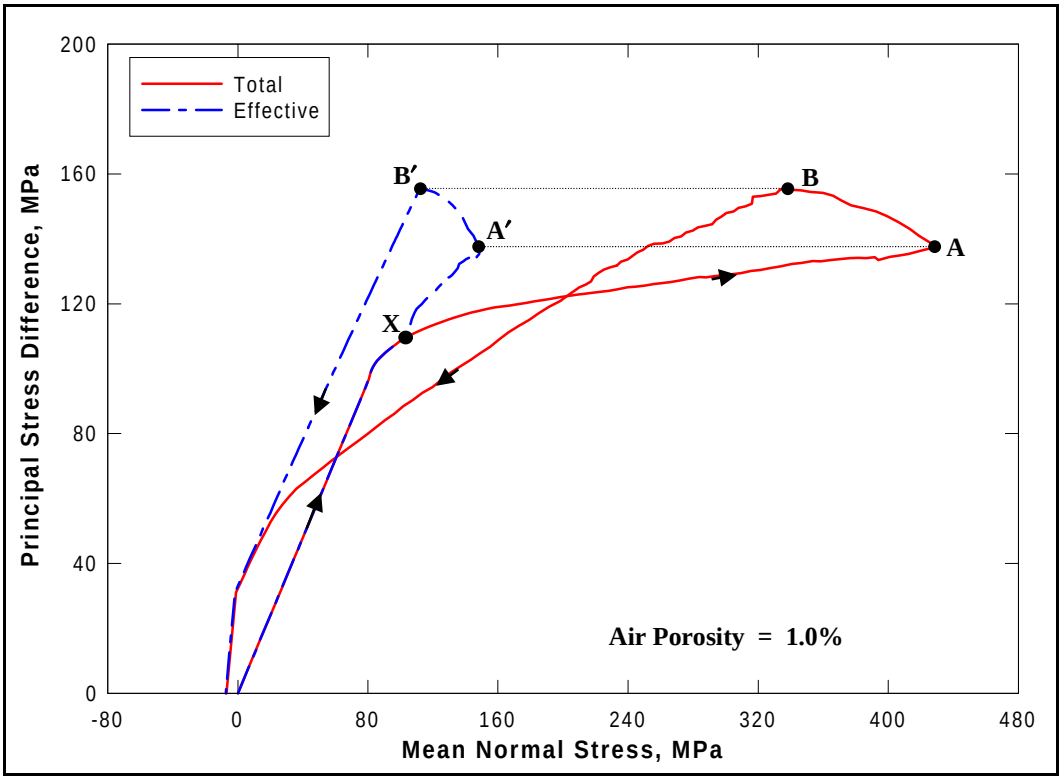

Figure 6.22. Stress paths from K_o/BX simulation at 1% air porosity

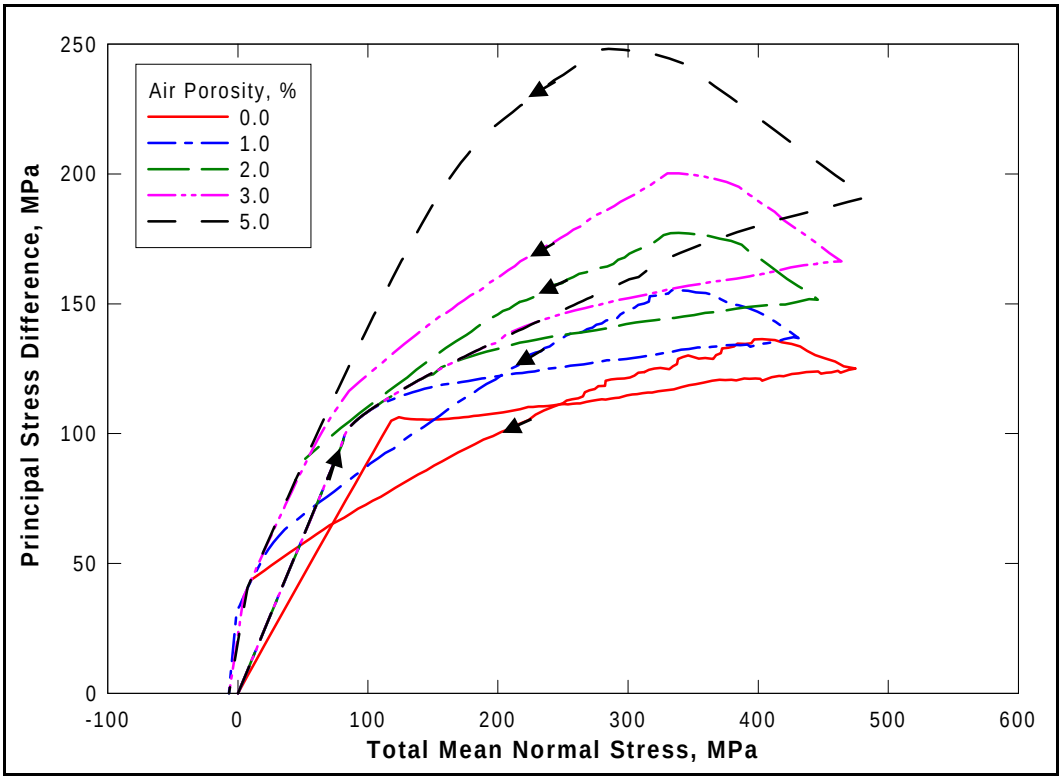

Figure 6.23. Total stress paths from five K_o/BX simulations

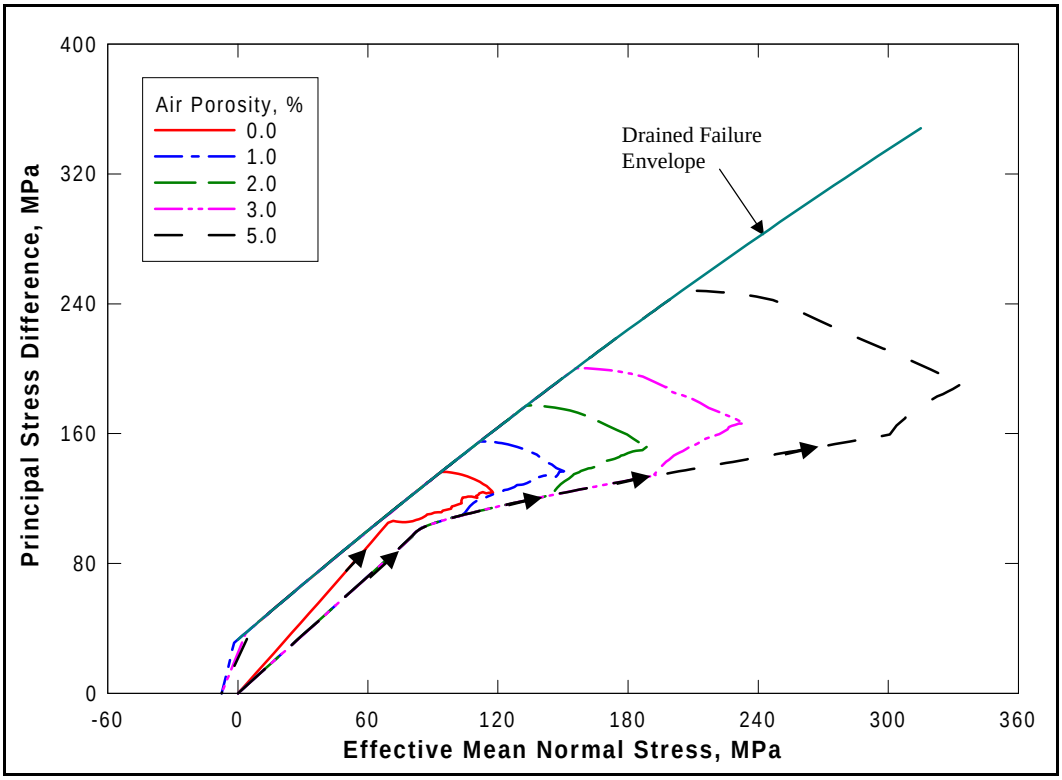

Figure 6.24. Effective stress paths from five K_o/BX simulations

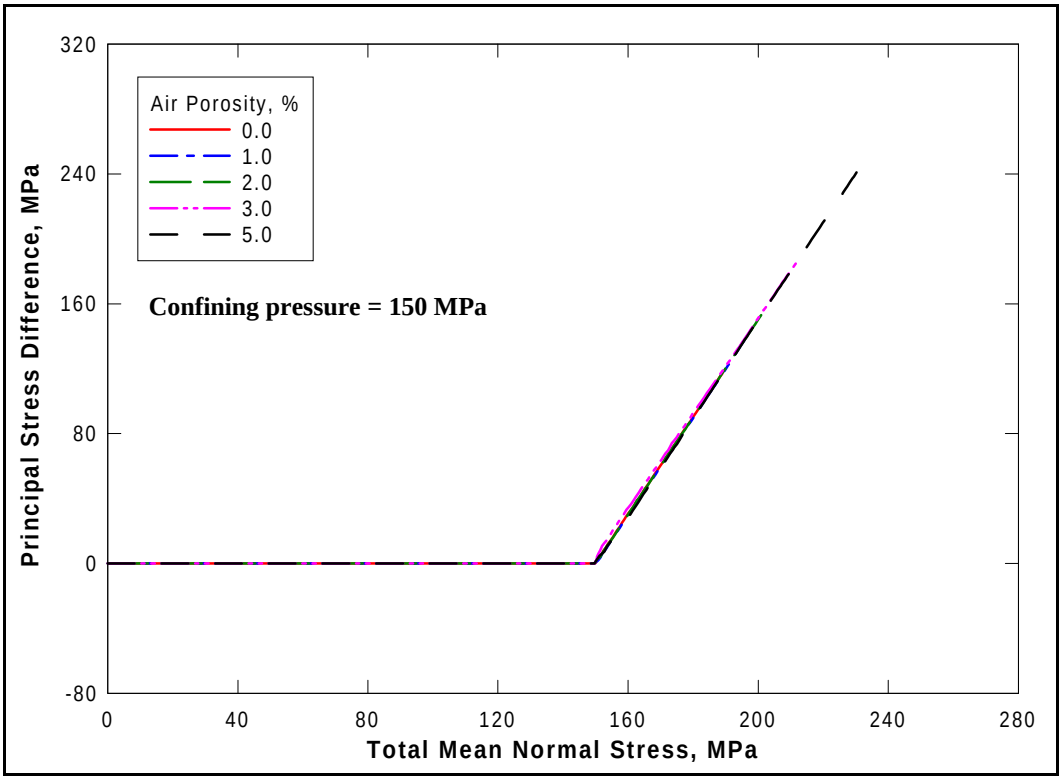

Figure 6.25. Total stress paths from five TXC simulations: confining pressure = 150 MPa

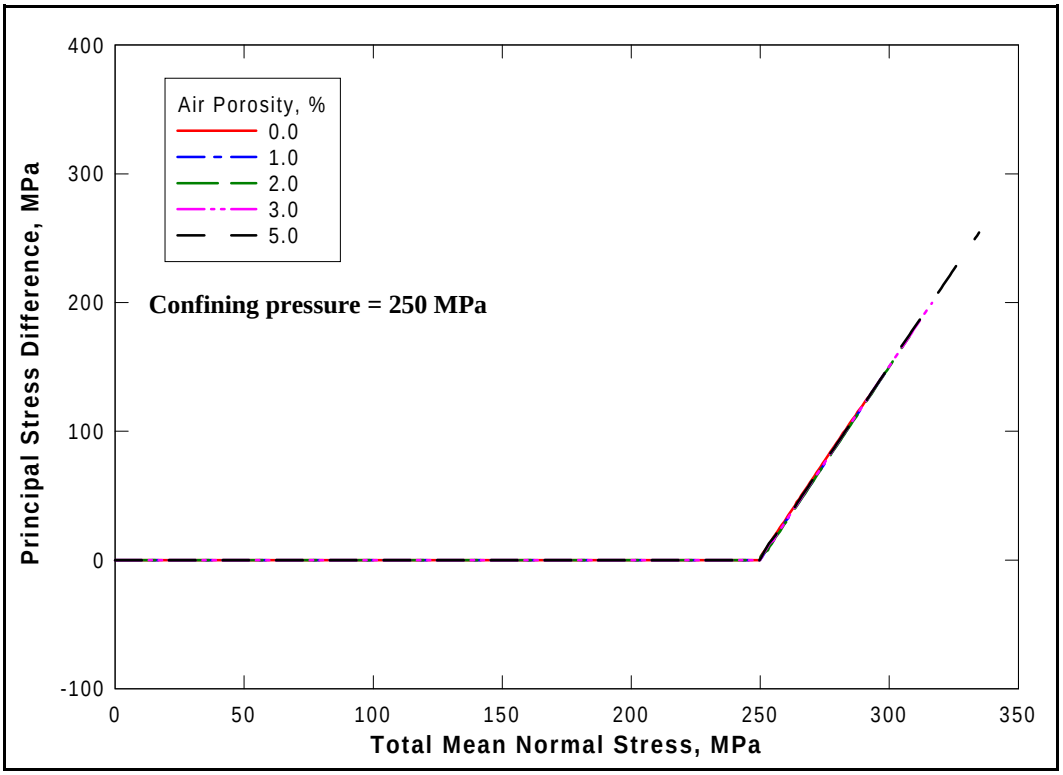

Figure 6.26. Total stress paths from five TXC simulations: confining pressure = 250 MPa

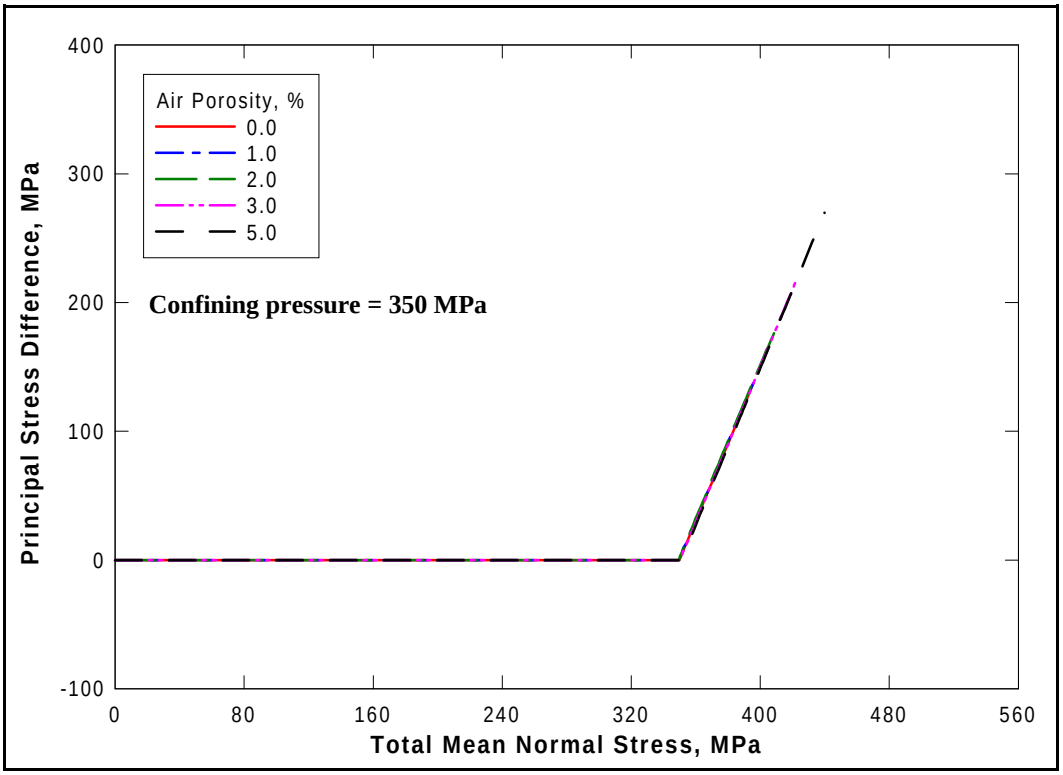

Figure 6.27. Total stress paths from five TXC simulations: confining pressure = 350 MPa

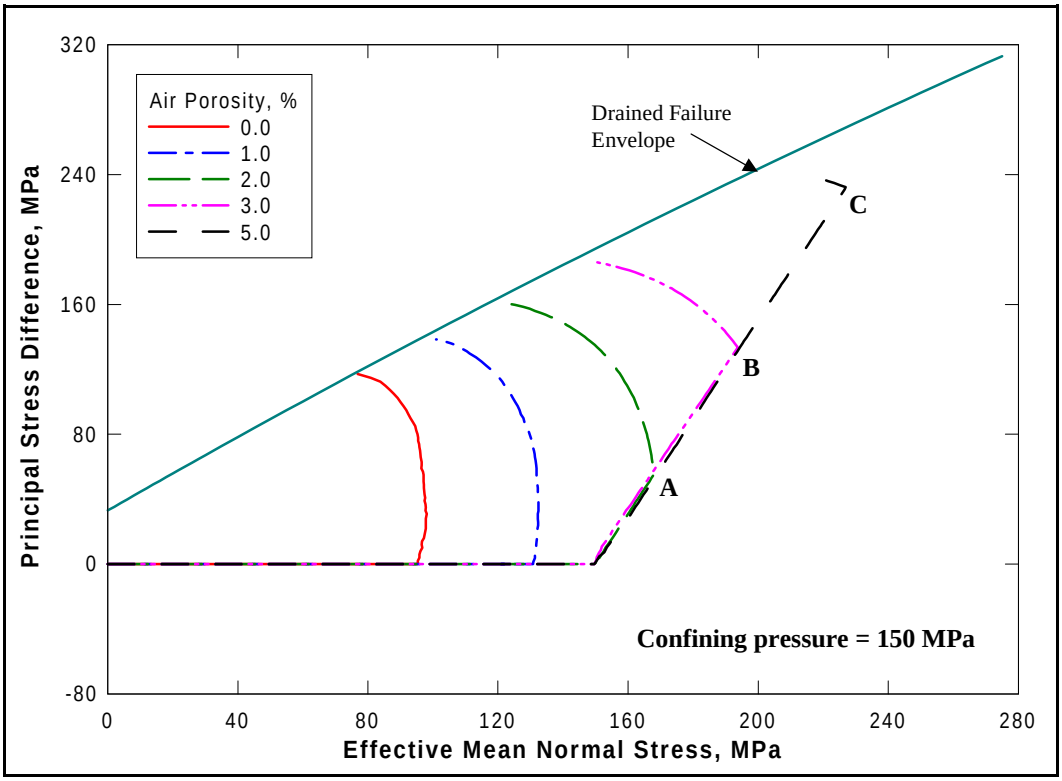

Figure 6.28. Effective stress paths from five TXC simulations: confining pressure = 150 MPa

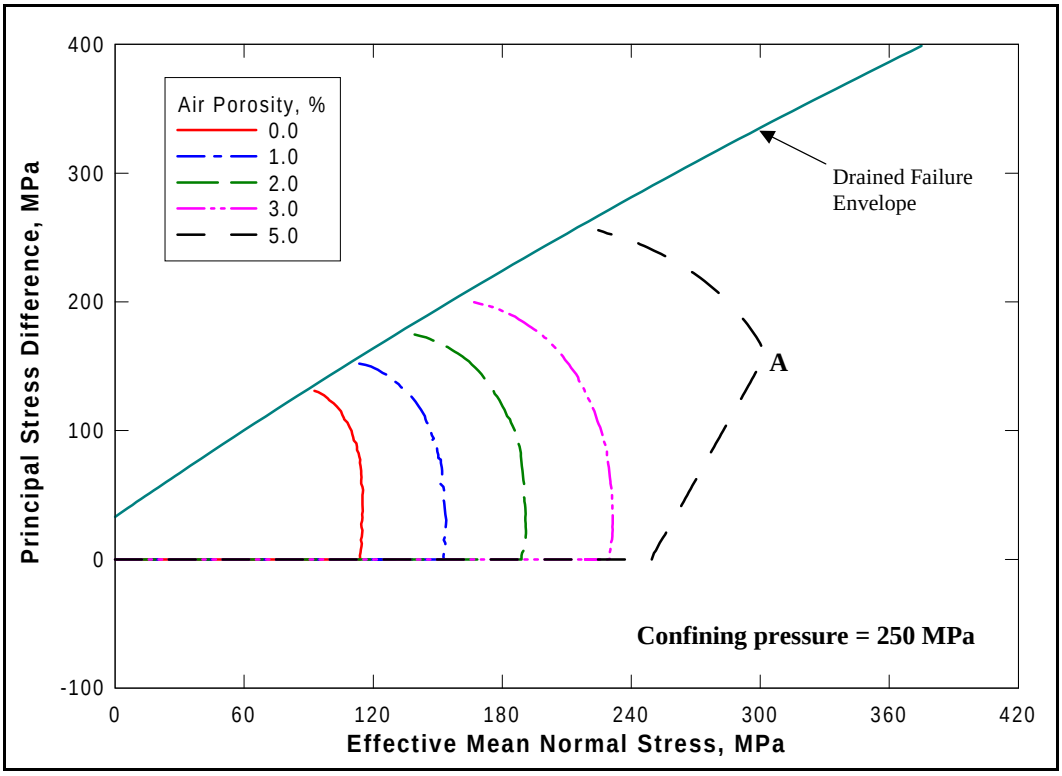

Figure 6.29. Effective stress paths from five TXC simulations: confining pressure = 250 MPa

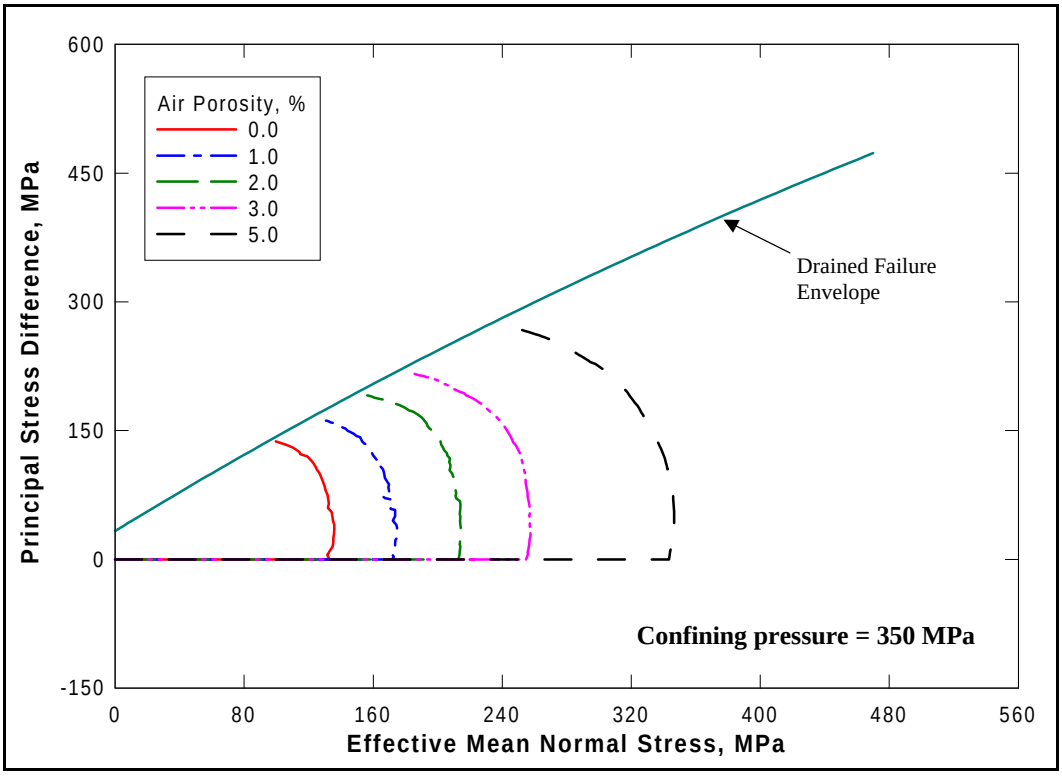

Figure 6.30. Effective stress paths from five TXC simulations: confining pressure = 350 MPa

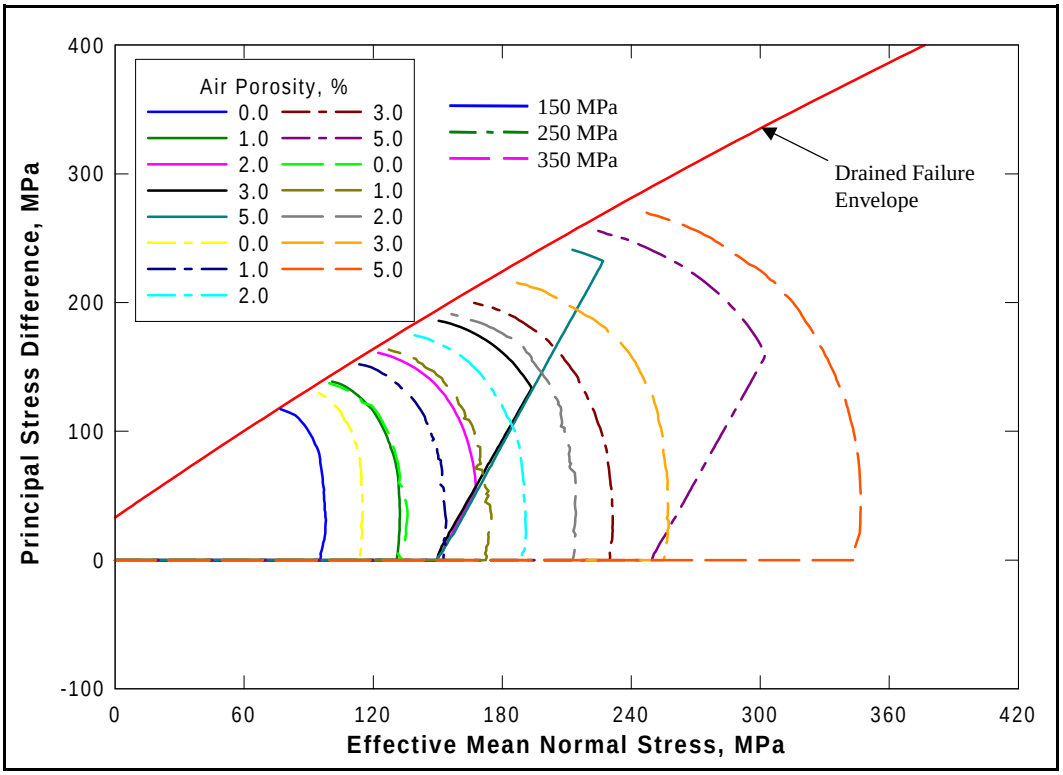

Figure 6.31. Effective stress paths from fifteen TXC simulations

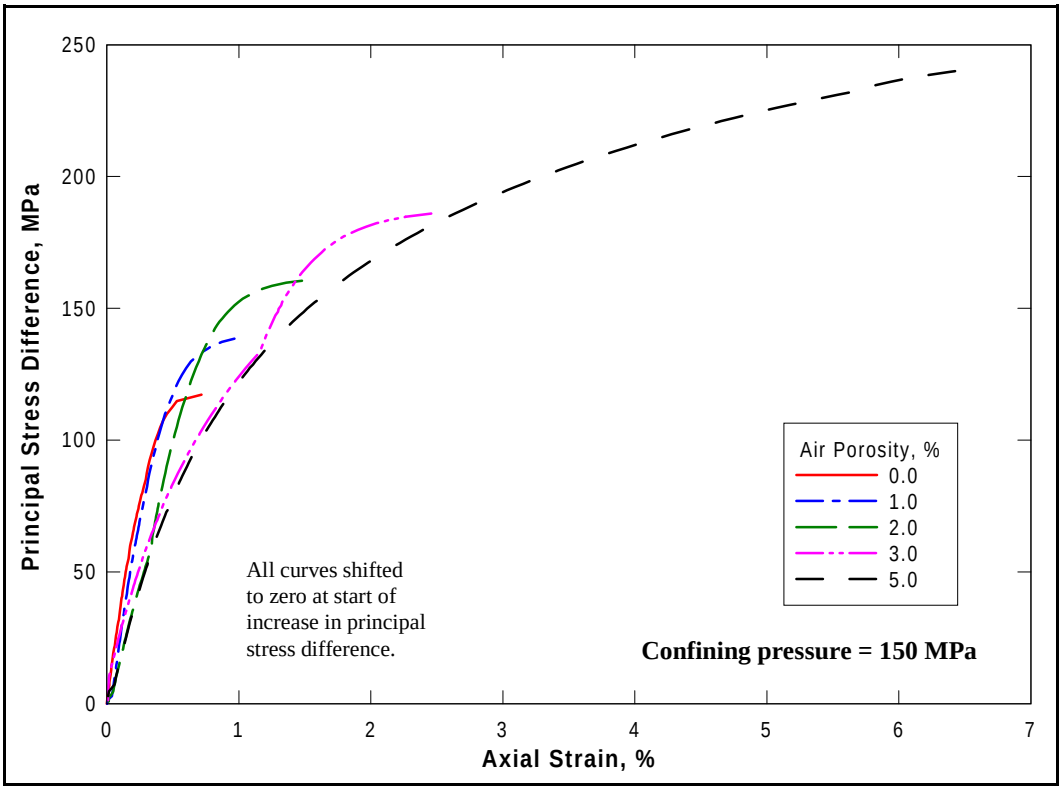

Figure 6.32. Stress-strain results from five TXC simulations: confining pressure = 150 MPa

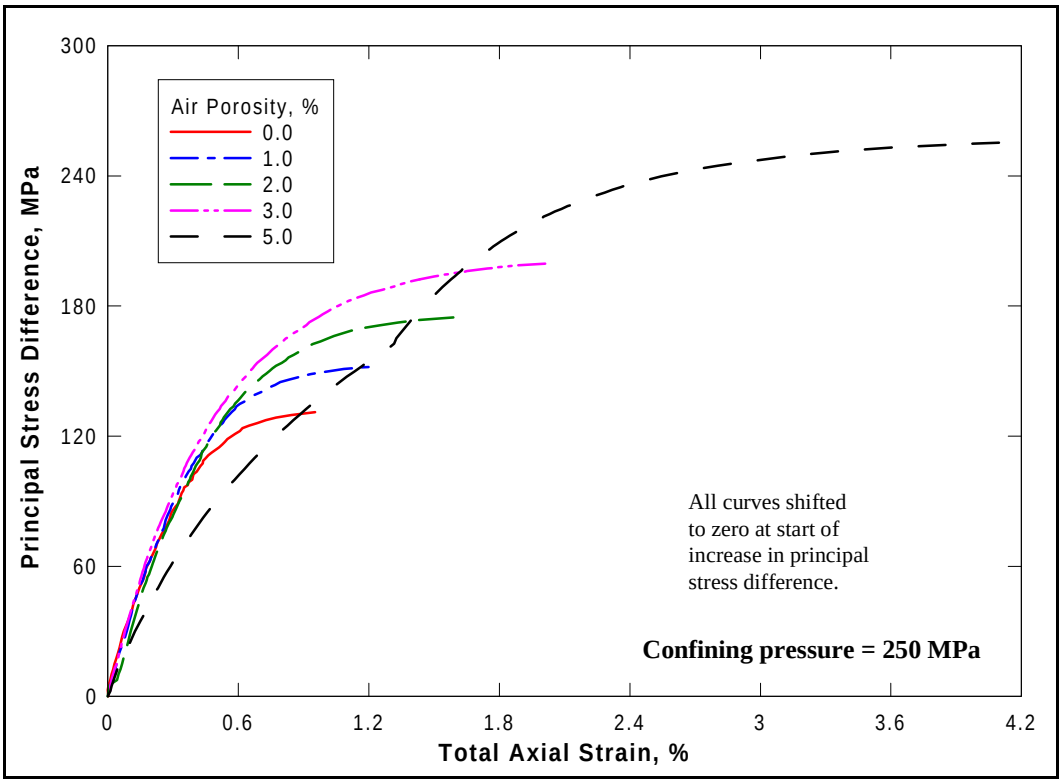

Figure 6.33. Stress-strain results from five TXC simulations: confining pressure = 250 MPa

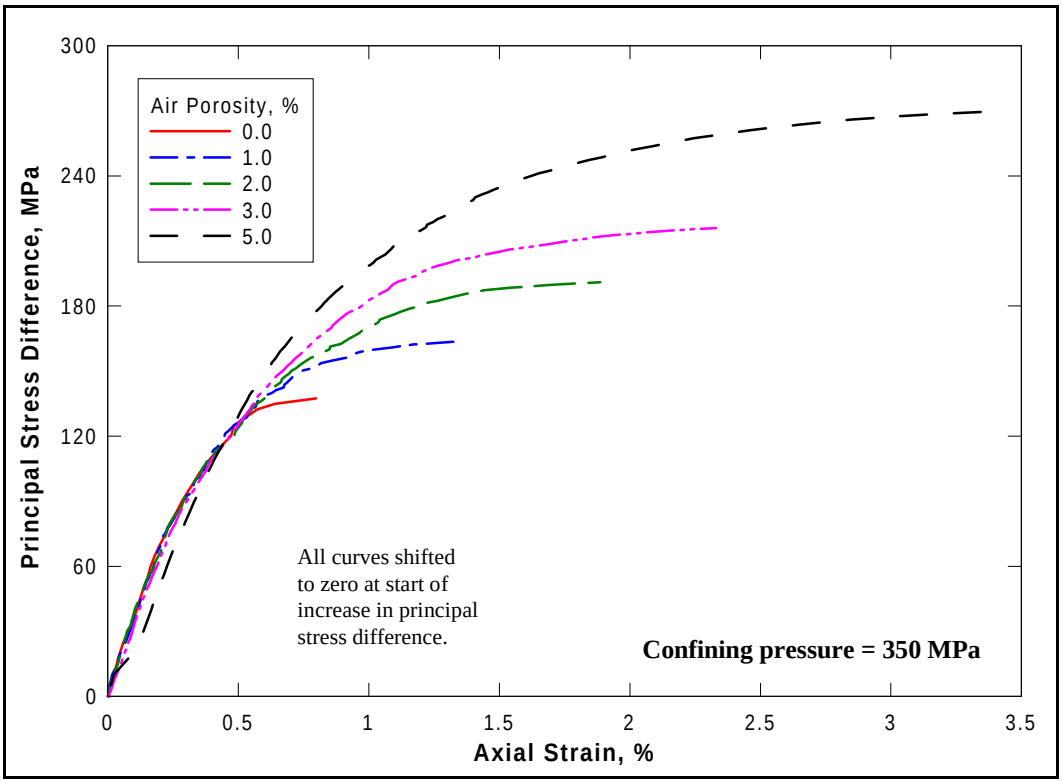

Figure 6.34. Stress-strain results from five TXC simulations: confining pressure = 350 MPa

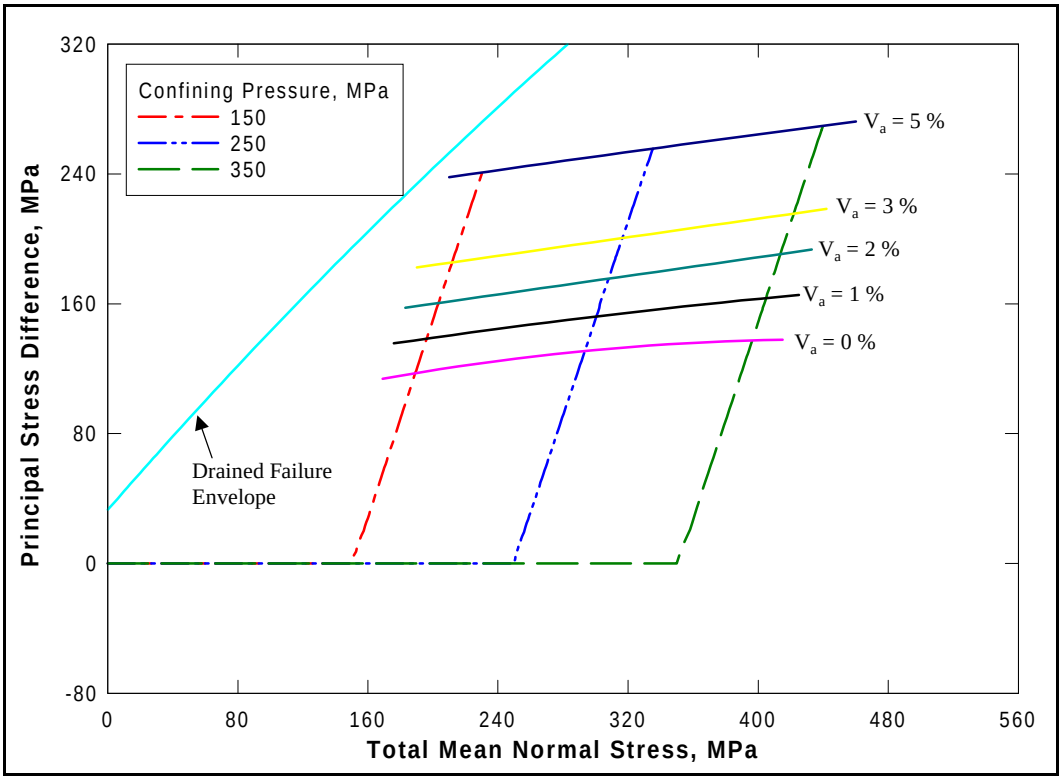

Figure 6.35. Undrained failure surfaces at five values of air porosity

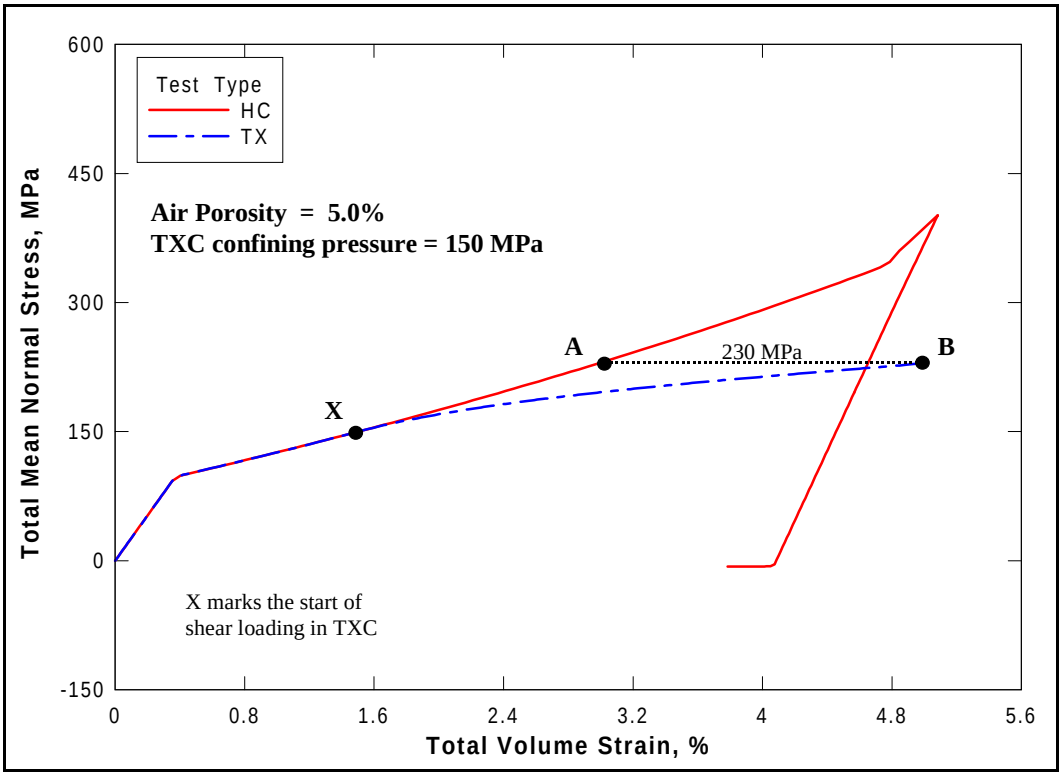

Figure 6.36. Pressure-volume results from HC and TXC simulations

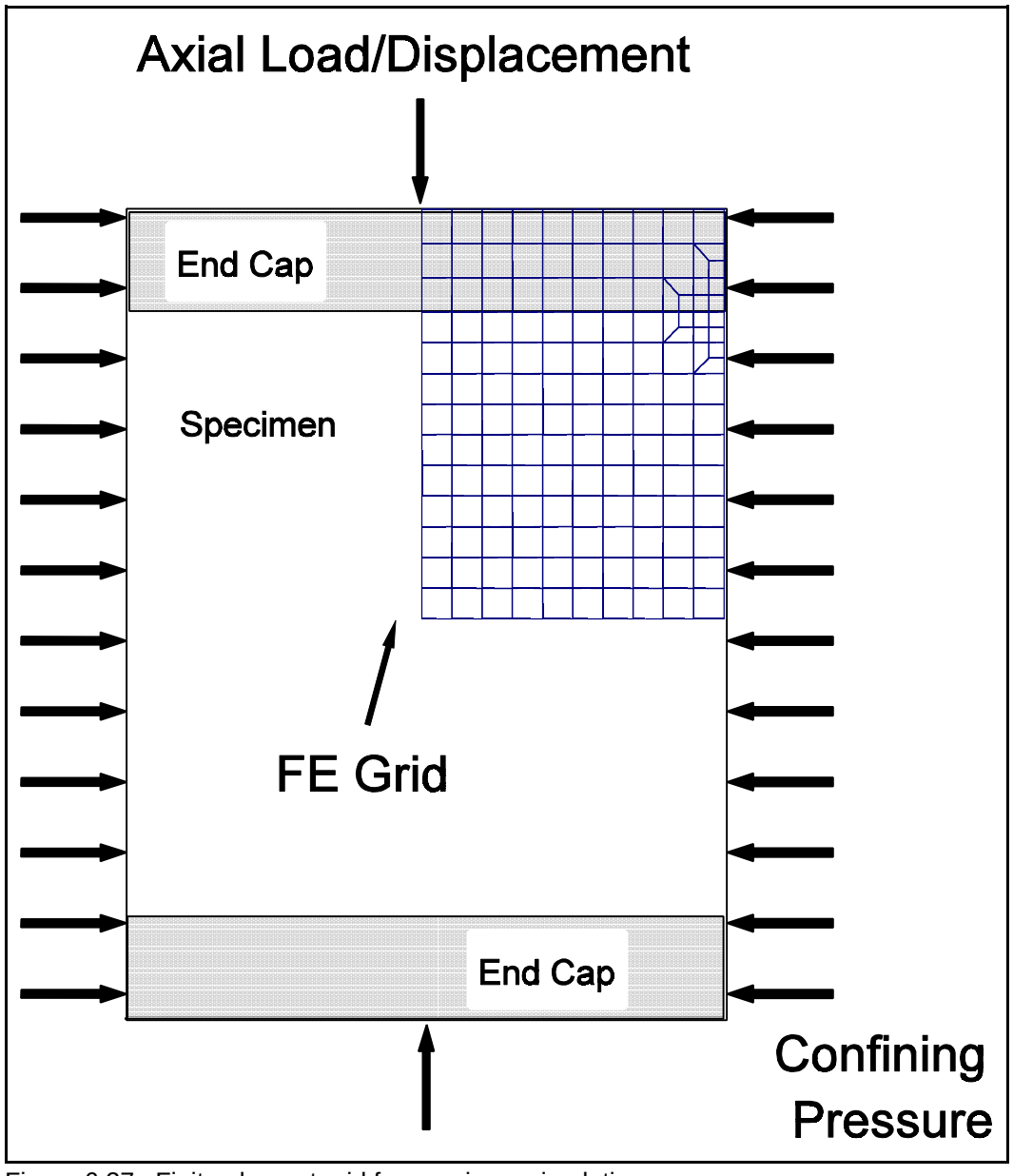

Figure 6.37. Finite element grid for specimen simulation

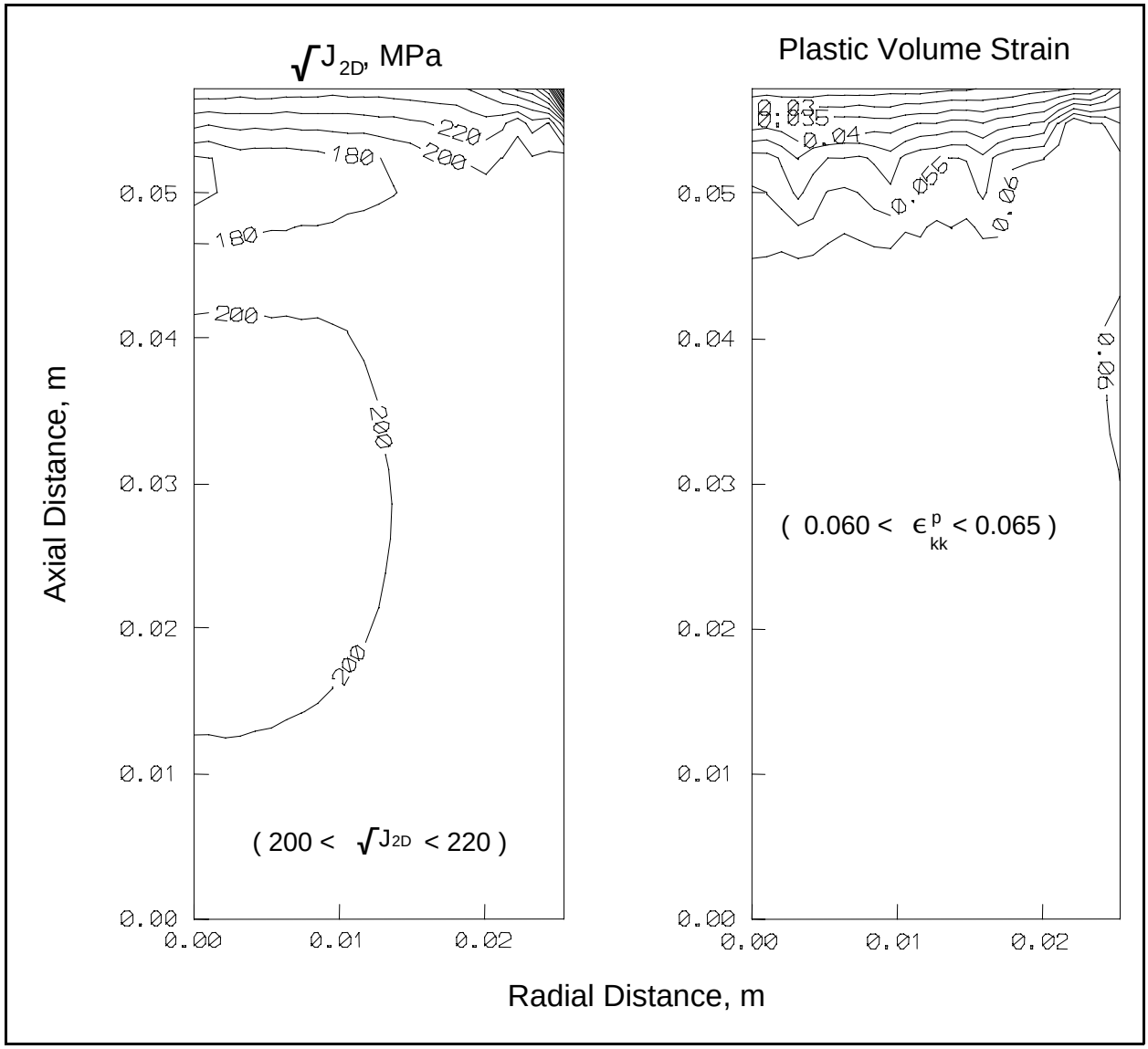

Figure 6.38. Contour plots of $\sqrt{J_{2D}}$ and plastic volume strain for a drained TXC test

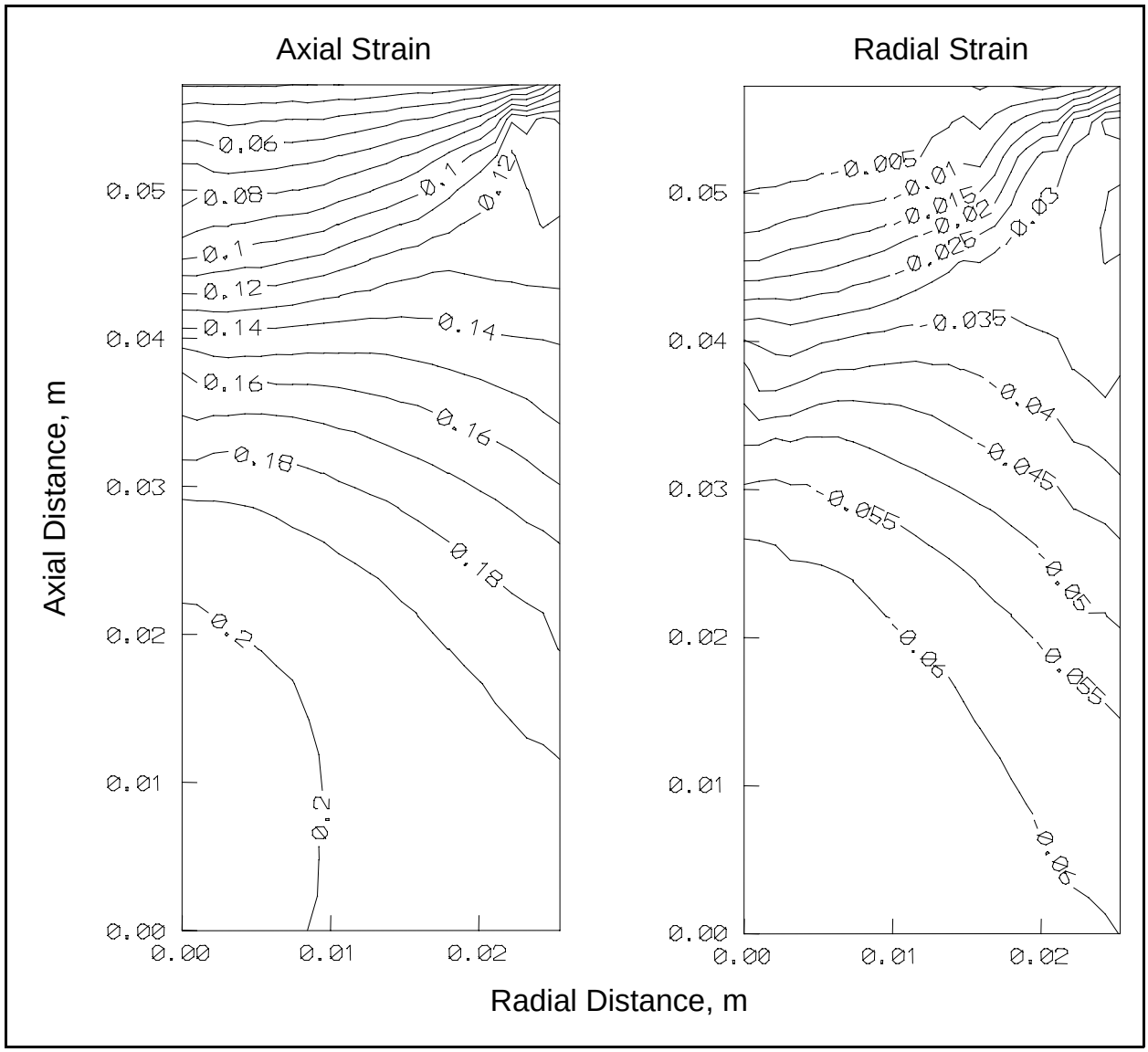

Figure 6.39. Contour plots of axial and radial strain for a drained TXC test

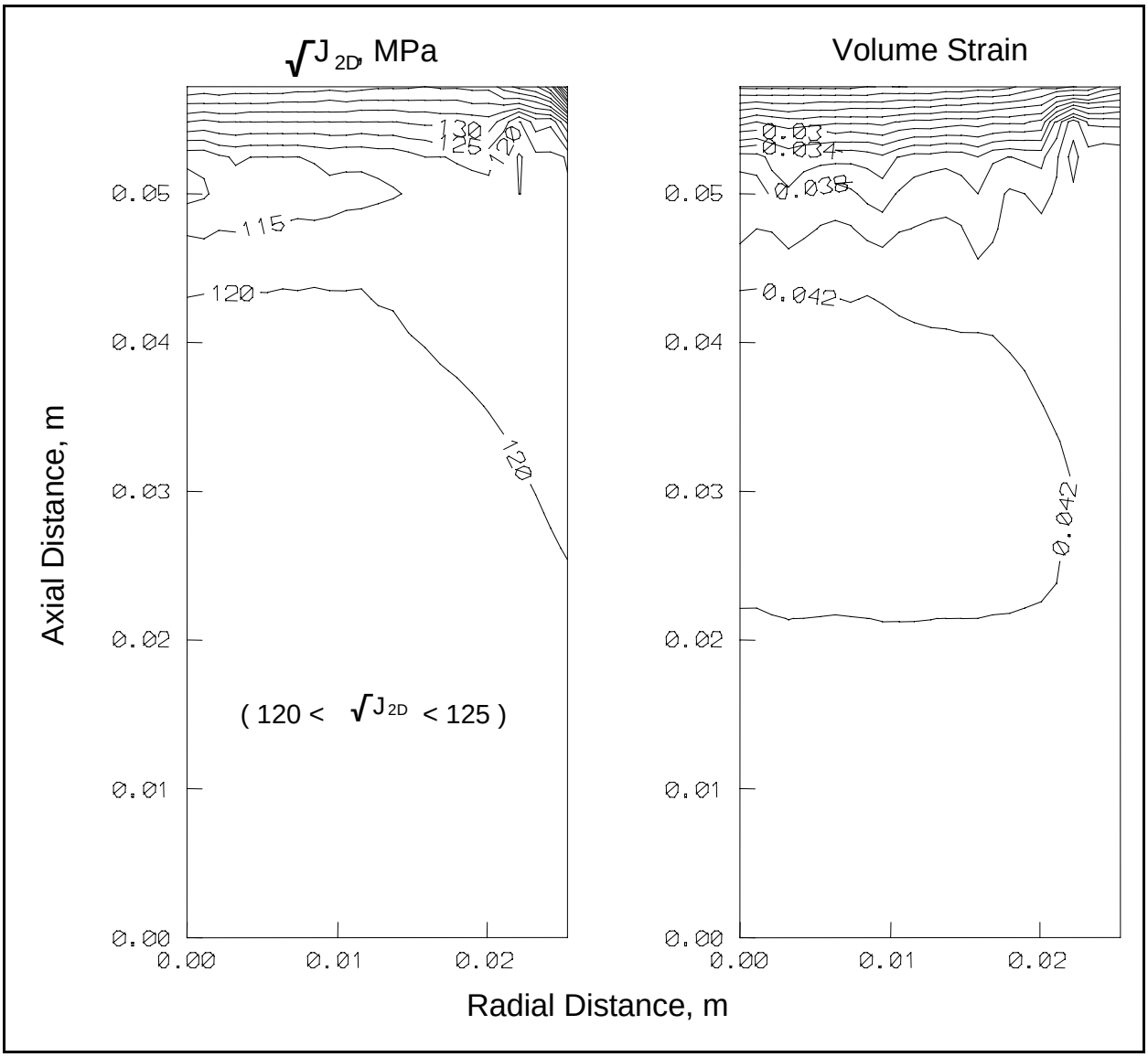

Figure 6.40. Contour plots of stress and volume strain.

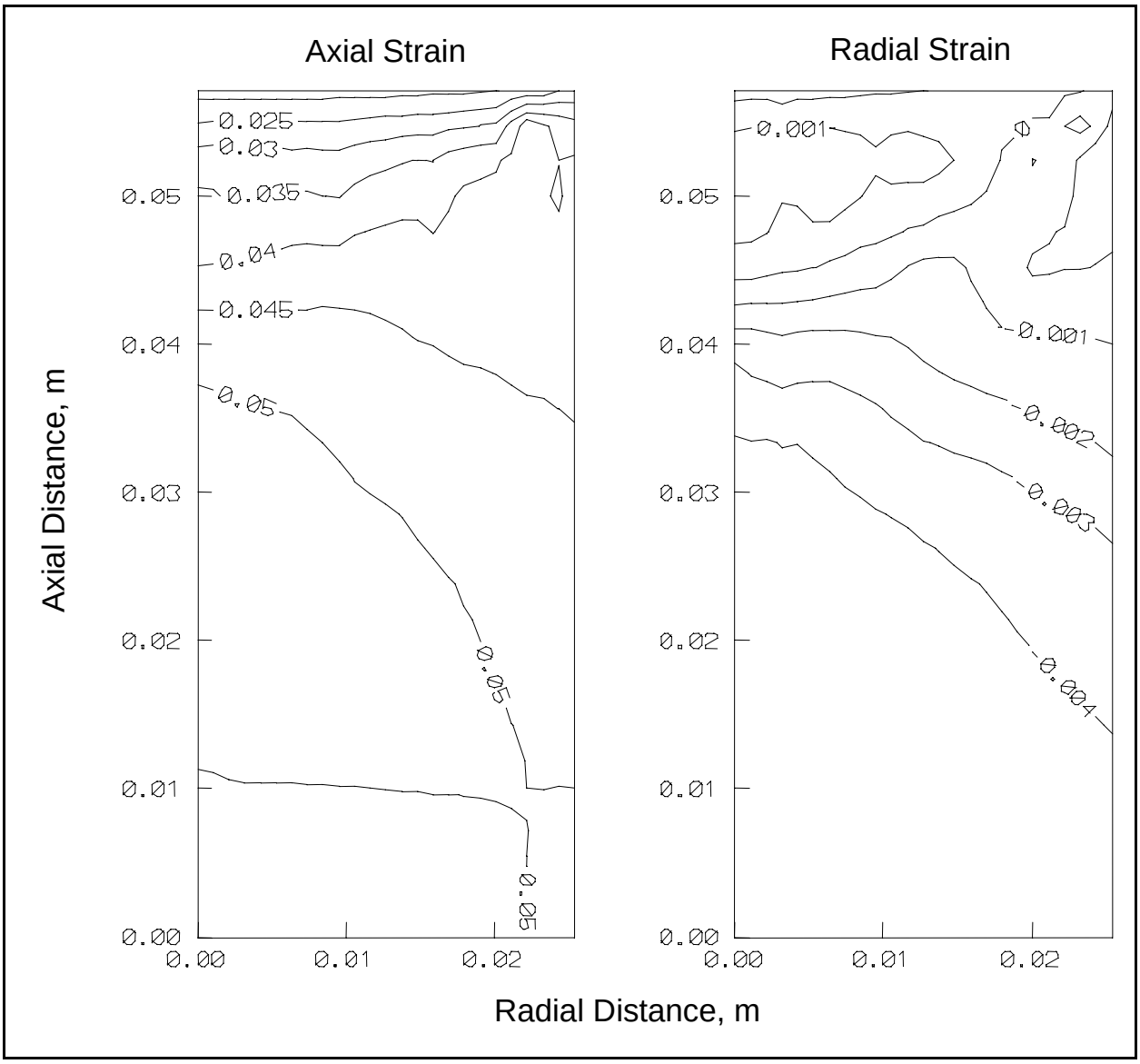

Figure 6.41. Contour plots of axial and radial strain.